JOURNAL OF PETROLOGY | VOLUME 0 | NUMBER 0 | PAGES 1–32 | 2012 | doi:10.1093/petrology/egs020
Journal of Petrology Advance Access published April 12, 2012

Timescales of Magma Recharge and Reactivation of Large Silicic Systems from Ti Diffusion in Quartz

N. E. MATTHEWS[1]*, C. HUBER[2], D. M. PYLE[1] AND V. C. SMITH[3]

[1]DEPARTMENT OF EARTH SCIENCES, UNIVERSITY OF OXFORD, SOUTH PARKS ROAD, OXFORD OX1 3AN, UK
[2]SCHOOL OF EARTH AND ATMOSPHERIC SCIENCES, GEORGIA INSTITUTE OF TECHNOLOGY, 311 FERST DRIVE, ATLANTA, GA 30332, USA
[3]RESEARCH LABORATORY FOR ARCHAEOLOGY AND THE HISTORY OF ART, UNIVERSITY OF OXFORD, SOUTH PARKS ROAD, OXFORD OX1 3QY, UK

RECEIVED MARCH 3, 2011; ACCEPTED FEBRUARY 16, 2012

Timescales of magma chamber assembly and recharge are investigated here by applying 1D and 2D diffusion modeling techniques to high-resolution maps of titanium in quartz from a large-volume ignimbrite eruption in the Taupo Volcanic Zone, New Zealand. We compare quartz zonation patterns and associated diffusion timescales from the ~340 ka Whakamaru super-eruption (magma volume ~1000 km^3) with the Younger Toba Tuff super-eruption, 74 ka (2000 km^3), Sumatra, and the smaller volume ~50 ka Earthquake Flat eruption (10 km^3), Okataina Caldera Complex, New Zealand. Two principal timescales are presented: that of chamber recharge and eruption triggering events, and that of magma generation (involving long-term assembly, stirring and reactivation). Synchrotron micro-X-ray fluorescence maps of core–rim quartz transects provide a high-resolution record of magma chamber conditions throughout quartz crystallization. Quartz crystals from the Whakamaru magma display complex zonation patterns indicating fluctuating pressure–temperature conditions throughout the crystallization history. Toba and Earthquake Flat, in contrast, display simple quartz-zoning patterns and record slightly longer periods of crystal residence in the chamber that fed the eruption. We apply Lattice Boltzmann 2D diffusion modeling to reconstruct the timescales of quartz crystal zonation, accounting for crystal boundary complexities. Quartz crystal orientation is also accounted for by using geometry constraints from the synchrotron data. Our calculations suggest that crystal-mush reactivation for the main Whakamaru magma reservoir occured over a period of the order of 10^3–10^4 years. Both the Earthquake Flat and Toba eruptions experienced a significant recharge event (causing a temperature and pressure change), which occurred within ~100 years of eruption. In comparison, the complex Whakamaru quartz zoning patterns suggest that the magma body experienced numerous thermal and compositional fluctuations in the lead-up to eruption. The final magma recharge event, which most probably triggered the eruption, occurred within ~10–60 years of the eruption. Even though the volume of these systems spans two orders of magnitude, there does not appear to be a relationship between magma volume and diffusion timescale, suggesting similar histories before eruption.

KEY WORDS: *diffusion; quartz; silicic magma; timescales; Taupo Volcanic Zone; Toba*

INTRODUCTION

A major goal in volcanology is to understand how super-eruptions (with magma volumes >500 km^3; Mason *et al.*, 2004) are triggered, the storage of these voluminous silicic melts, and the timescales over which these processes occur. Current understanding is that these highly evolved melts are at least partially generated in the upper crust from crystal-rich mush zones (Hildreth, 1981; Bachmann & Bergantz, 2004). The clues to the cause of eruptions of these large volumes of silicic melt can be found in the erupted products, in particular in the records of pressure and temperature changes that are encoded in the

*Corresponding author. Present address: US Geological Survey, MS 910, 345 Middlefield Road, Menlo Park, CA 94025, USA.
E-mail: nmatthews@usgs.gov

compositions of crystallizing phases. In addition to magmatic processes occurring in the reservoir, caldera eruptions may also be triggered by tectonic forces, which may cause destabilization of the system (e.g. Gottsmann *et al.*, 2009; Petrinovic *et al.*, 2010). Quartz is a ubiquitous mineral phase in pumice erupted during super-eruptions, and although quartz crystals appear homogeneous optically, complex zoning patterns are revealed by cathodoluminescence (CL) imaging. CL zonation may be interpreted in terms of temperature and pressure changes during mineral growth within the melt body (Peppard *et al.*, 2001; Wark & Watson, 2006; Thomas *et al.*, 2010; Matthews *et al.*, 2012); but the extent to which such CL patterns faithfully record mineral composition (particularly Ti content) and temperature is unknown.

The rates and timing of pre-eruption magmatic processes occurring in large-volume magma chambers are poorly known, and yet this information is essential for understanding and quantifying these magmatic systems. Diffusion modeling of chemical gradients in minerals is an important chronological tool that can provide constraints on the timing and duration of thermal–chemical and eruption-triggering events. Kinetic modeling tools have been applied to investigate timescales and processes in a range of volcanic settings (e.g. Nakamura, 1995; Zellmer *et al.*, 1999; Coombs *et al.*, 2000; Klügel, 2001; Costa & Chakraborty, 2004; Morgan *et al.*, 2004; Shaw, 2004; Costa & Dungan, 2005; Morgan & Blake, 2006; Costa *et al.*, 2008, 2010). High-resolution compositional profiles across zoned crystals can be used to determine the residence times of crystals at magmatic temperatures, using known diffusion rates for the element under consideration. This temporal information can then be linked with the magmatic processes responsible for generating the compositional changes.

Here we build on our TitaniQ geothermometery results (presented by Matthews *et al.*, 2012) together with interpretations of CL images (Watt *et al.*, 1997; Götze *et al.*, 2001, 2004; Peppard *et al.*, 2001), geothermometry, and high-resolution micro-X-ray fluorescence (μ-XRF) synchrotron Ti maps of quartz crystals extracted from the Whakamaru Group Ignimbrites and Earthquake Flat (EQF) deposits, Taupo Volcanic Zone (TVZ), New Zealand (Fig. 1), and the Younger Toba Tuff (YTT), Sumatra (Fig. 2). Both 1D modeling and 2D Lattice Boltzmann diffusion modeling techniques (see Huber *et al.*, 2010*a*) are applied to Ti in quartz to model timescales associated with a significant thermal–pressure event recorded in quartz rims. This comparison of quartz-zoning timescales from Whakamaru with those from the smaller EQF eruption (Okataina Caldera Complex, OCC) and the larger YTT super-eruption allows us to test whether or not the magnitude of eruption and source magma chamber volume correlate with quartz zoning and the related timescales.

The primary objectives of this new study were to: (1) measure the spatially resolved Ti content of representative zoned quartz crystals to test the assumption that CL zoning in volcanic quartz is caused by compositional zoning of Ti; (2) use spatially resolved (<4 μm) measurements of Ti across zoned quartz to reconstruct changes in magma chamber conditions prior to eruption; (3) use 1D and 2D diffusion modeling techniques to estimate timescales of magma chamber processes required to explain gradients in Ti content across critical growth zones of volcanic quartz crystals. This information allows us to assess timescales of pre-eruption pressure and temperature changes in the large-volume magma bodies, and therefore to understand how the systems were assembled and triggered.

REGIONAL GEOLOGY

The TVZ (Fig. 1) is an actively rifting arc that has produced rhyolite eruptions at millennial frequency during the late Quaternary (Wilson *et al.*, 1995, 2009), making it the ideal area for studying the processes governing the production, storage and eruption of rhyolite magma. Mesozoic basement greywackes crop out east and west of the TVZ and underlie the volcanic fill within the zone, either as rifted blocks with intrusions or as tectonically stretched crust (Stern *et al.*, 2006). The very high heat flux (total heat flux per kilometer of strike is 4×10^7 W km^{-1} in the central, rhyolite-dominated portion of the TVZ: Bibby *et al.*, 1995; Hochstein, 1995) causes the brittle-to-ductile transition to occur at 6–7 km depth (Bryan *et al.*, 1999), and seismic refraction data indicate that the quartzo-feldspathic upper crust extends to 15–16 km depth (Harrison & White, 2004; Stratford & Stern, 2004). The low P-wave velocities (6·9–7·3 km s^{-1}; Stratford & Stern, 2004) below 15–16 km may represent mantle with significant amounts of melt, or highly intruded mafic crust with ~2% melt (Harrison & White, 2004).

Eruptions in the central TVZ are volumetrically dominated by rhyolite magma, with lesser amounts of andesite > dacite > basalt as surficial eruptive units (Cole, 1990; Wilson *et al.*, 1995). Isotopic data indicate that the silicic melts are generated from highly fractionated primitive basalt that has been contaminated by the metasedimentary crust (<25%; McCulloch *et al.*, 1994; Graham *et al.*, 1995), although there is also evidence for silicic components derived from direct crustal melting (Charlier *et al.*, 2008, 2010). The high volumes of mafic magma required to generate the rhyolites, by whatever pathway of fractionation or crustal melting may apply, are almost entirely trapped within or immediately below the quartzo-feldspathic crust. A characteristic feature of the central TVZ is, however, that mafic melts do reach and interact with the melt-dominant magma bodies at shallow (4–8 km) depths and are not entirely

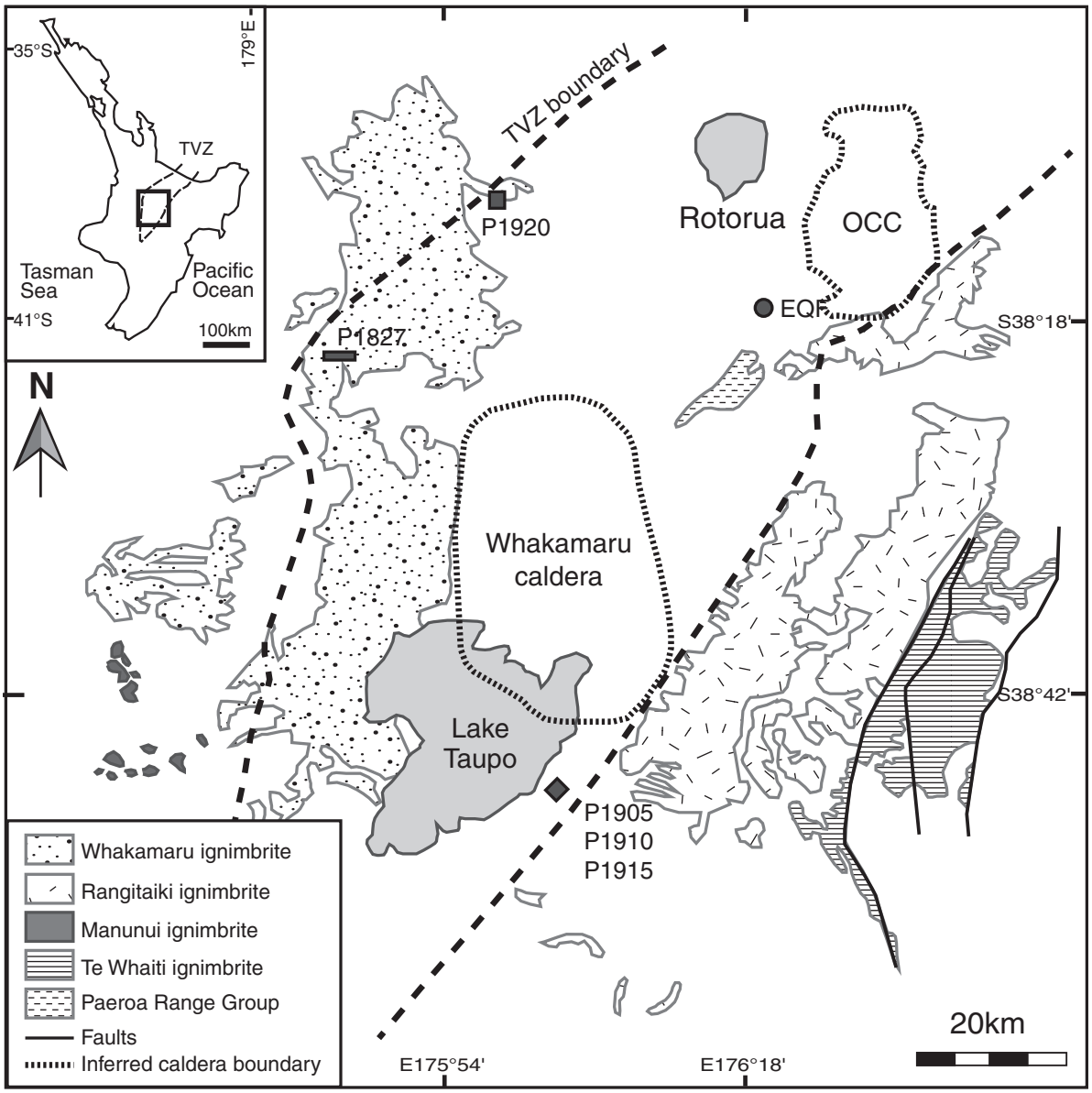

Fig. 1. Distribution of Whakamaru Group ignimbrites; inset shows TVZ, North Island, New Zealand. Whakamaru caldera boundary outlined by wide dotted black line; TVZ boundary marked by black dashed line; OCC, Okataina Caldera Complex. Sample localities and sample codes: P1905, P1910 and P1915 are Rangitaiki pumices; P1920 and P1827 are Whakamaru; EQF, Earthquake Flat pumice. Modified from Brown et al., 1998 and Matthews et al., 2012.

confined within a deeper mush zone (see Hildreth, 1981, 2004). Mafic magma evidently interacted with the dominant silicic melt that fed the Rangitaiki member of the Whakamaru deposits (Brown *et al.*, 1998; Matthews *et al.*, 2012; this study), and there is evidence for mafic interaction prior to many of the younger rhyolite eruptions of the Taupo and Okataina volcanoes (Blake *et al.*, 1992; Leonard *et al.*, 2002; Wilson *et al.*, 2006; Shane *et al.*, 2007, 2008*b*).

WHAKAMARU GROUP IGNIMBRITES

The Whakamaru eruption occurred at ~340 ka, and involved >1000 km^3 of rhyolitic magma (Wilson *et al.*, 1986; Brown *et al.*, 1998). The resulting ignimbrites cover ~13 000 km^2 of central North Island (Fig. 1) and have been previously characterized by field, petrological and geochemical investigations (Ewart, 1965; Martin, 1965;

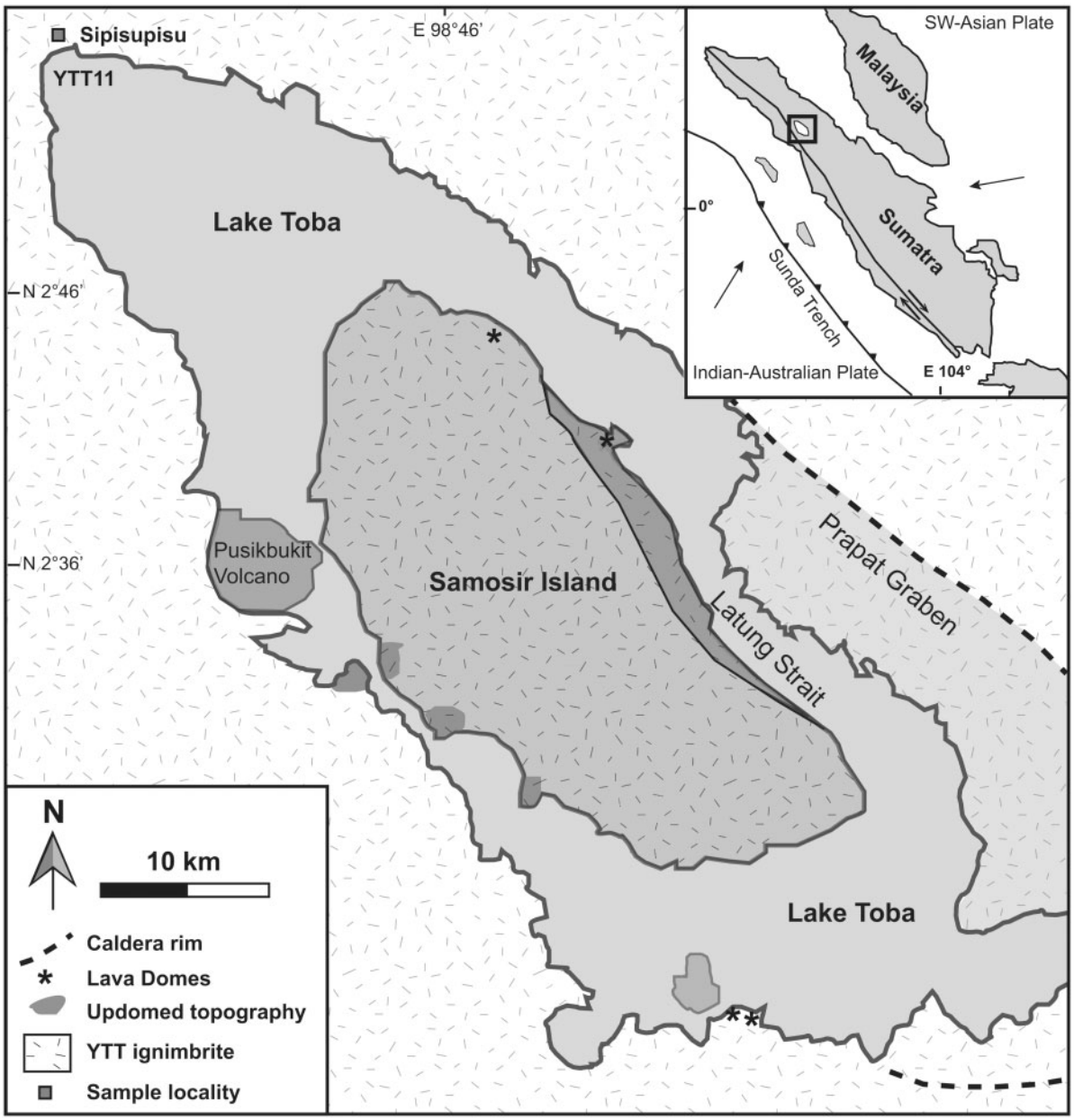

Fig. 2. Map showing main structural and topographic features of the Toba Caldera Complex. Inset shows tectonic setting and location map with relative vectors of plate movement indicated by arrows; rectangle indicates the location of the detailed map. Recent areas of updoming along the western lake shore are associated with hydrothermal and fumarolic activity. Proximal YTT sample locality marked (at Sipisupisu township). Adapted from Chesner (1998).

Briggs, 1976; Wilson *et al.*, 1986; Brown *et al.*, 1998; Brown & Fletcher, 1999). The deposit comprises five crystal-rich (~15–30% crystal content) ignimbrite units named the Whakamaru, Manunui, Rangitaiki, Te Whaiti and Paeroa Range Group ignimbrites (Fig. 1; Brown *et al.*, 1998). Field evidence suggests that these multiple eruptions occurred over a geologically short time period (<10 kyr; Brown *et al.*, 1998). These units share similar ranges in geochemistry and petrography, and each contains varying amounts of five distinct pumice (magma) types (classified as types A, B, C, D and mixed basaltic on the basis of different compositions and crystal contents; Brown *et al.*, 1998; Matthews *et al.*, 2012). The presence of these distinct magma compositions suggests complex crystallization processes in multiple magma chambers. Brown *et al.* (1998) provided evidence that the less evolved, low-silica rhyolites

underwent significant fractionation at shallow crustal levels to produce the more evolved rhyolites that were ultimately erupted. The mixed and mingled basaltic pumice clasts provide direct evidence for a basaltic recharge event prior to eruption (see Matthews *et al.*, 2012). Our previous analysis of quartz zoning demonstrated that the Whakamaru eruption was preceded by a major temperature rise (~100°C) or pressure drop, associated with mafic recharge, which rejuvenated the crystal mush and triggered eruption (Matthews *et al.*, 2012). This study focuses on the timescales over which these open-system processes occurred prior to eruption.

EARTHQUAKE FLAT ERUPTION

The EQF eruption episode occurred at ~50 ka, immediately following the Rotoiti eruption (~120 km^3) from the OCC (Fig. 1). The eruption involved ~10 km^3 of rhyolitic magma erupted from vent localities at the southern margin of the Kapenga caldera, which overlaps with the structural boundary of the larger OCC structure (Smith *et al.*, 2005). The EQF deposits are silicic and crystal-rich (25–45%) with a mineral assemblage dominated by hornblende and biotite (Smith *et al.*, 2010), and with compositional similarities to the earlier Rotoiti magma (Schmitz & Smith, 2004). Zircon age spectra indicate that they had a separate crystallization history from the Rotoiti magma reservoir (Charlier *et al.*, 2003), and hornblende textural and chemical variations suggest that there was a thermal event immediately prior to the eruption that caused rejuvenation of a crystal-rich system and triggered eruption (Molloy *et al.*, 2008). Volatile contents and plagioclase and quartz zonation in the EQF deposits have been discussed by Smith *et al.* (2010) and we build on this dataset by analyzing the same well-characterized crystals.

YOUNGER TOBA TUFF ERUPTION

The ~74 ka YTT eruption is one of the largest known eruptions on Earth. Approximately 3000 km^3 of magma was erupted from the Toba caldera in central Sumatra, Indonesia, forming the 100 km × 30 km caldera (Rose & Chesner, 1990; Chesner & Rose, 1991; Chesner, 1998; Vazquez & Reid, 2004; Fig. 2). Rhyolitic YTT tephra was dispersed throughout the Indian subcontinent, Indian Ocean, the Bay of Bengal, the Andaman Sea, and on land in Malaysia (Shane *et al.*, 1995; Liu *et al.*, 2006*b*). YTT glass is dominantly of high-silica rhyolite composition (e.g. Shane *et al.*, 1995; Chesner & Luhr, 2010; Smith *et al.*, 2011) and the proximal pumice is crystal-rich with up to 40 wt % crystals of quartz, sanidine, plagioclase, biotite and amphibole, with minor magnetite, ilmenite, allanite, zircon, fayalite and orthopyroxene (Chesner, 1998). Magma erupted during the past 1·2 Myr from the Toba caldera was compositionally zoned, ranging from rhyodacite to rhyolite, attributed to extensive fractional crystallization in the convecting magma body (Chesner, 1998). Crystallization of the quartz-bearing magma occurred at 700–760°C at depths of ~10 km (Chesner, 1998).

SAMPLES AND METHODS

Pumices from non-welded parts of the Whakamaru and Rangitaiki ignimbrites were sampled extensively (140 samples) and characterized by whole-rock XRF, matrix-glass and mineral chemistry (analysed using an electron microprobe and laser-ablation inductively coupled plasma mass spectrometry, LA-ICP-MS) and previously published Fe–Ti oxide compositional data (see supplementary data of Matthews *et al.*, 2012). Five pumice samples (three Rangitaiki and two Whakamaru; sample localities in Fig. 1) were selected for a detailed quartz CL study. Pumices were selected on the basis of mineralogy, clast size, degree of alteration and major element geochemistry. Pumice samples from the EQF (Fig. 1) and the YTT eruptions were selected for comparative purposes. The YTT sampling location is shown in Fig. 2. We used pumice fragments as these are considered to represent quenched fragments of the vesiculated rhyolite magma, with variations in glass composition between pumices reflecting variations within the parent magma reservoir(s) that were frozen in at the time of eruption. Details of the pumice samples referred to in this study are provided in Table 1.

Quartz crystals were extracted from each pumice clast by lightly crushing, sieving and hand-picking under an optical microscope. Single quartz fragments were chosen such that the glass selvedges were still intact on at least one face of the fragments, to best ensure that the complete core-to-rim crystal zonation was captured (although we note that the true cores may not be exposed owing to sectioning). These were mounted in epoxy resin, polished and carbon coated for imaging and analysis. Backscattered-electron (BSE) images of the mounts were made for ease of navigation, using a JEOL SEM in the Department of Earth Sciences, University of Oxford. Approximately 40 quartz crystals from each pumice sample were extracted, of which 92 were imaged by CL and analyzed using an electron microprobe as described below. A selection of 40 representative crystals was compositionally mapped using synchrotron μ-XRF.

Glass major and trace elements

Major element data were acquired, using a JEOL 8600 wavelength-dispersive electron microprobe (EMPA) at the Research Laboratory for Archaeology and the History of Art, University of Oxford, for glass shards separated from <150 μm fractions of crushed pumice, mounted in epoxy blocks and polished. LA-ICP-MS analysis of 26 petrogenetically significant trace elements in glass

Table 1: Summary of single pumice samples used in this study

Eruption unit	Sample code	Location	SiO_2 glass (wt %)	a_{TiO_2}	Quartz Ti (ppm)	TitaniQ T (°C)
Rangitaiki	P1905	38°52′09·5219″S, 176°03′13·1396″E	70·35	0·6	70–230	766–939
Rangitaiki	P1910	38°52′09·5219″S, 176°03′13·1396″E	70·40	0·5	60–190	770–938
Rangitaiki	P1915	38°52′09·5219″S, 176°03′13·1396″E	67·57	0·5	60–230	770–971
Whakamaru	P1920	38°12′19·9498″S, 175°55′35·4493″E	71·28	0·6	60–230	747–939
Whakamaru	P1827	38°19′30·6000″S, 175°41′03·5658″E	72·85	0·6	50–150	726–871
Younger Toba Tuff	YTT11	02°55′00·6″N, 98°31′20·9″E	74·53	0·5	11–214	594–958
Earthquake Flat	EQF1	38°15′53·336″S, 176°19′32·892″E	71·28	0·4	41–133	750–915

TitaniQ temperatures were calculated using the formulation of Wark & Watson (2006). The activity of Ti in the melt, a_{TiO_2}, was calculated using Fe-Ti compositional data, following the method of Reid et al. (2010). EQF data are from Smith *et al.* (2010); YTT a_{TiO_2} was calculated using Chesner (1998) Fe-Ti oxide data; Glass SiO_2 and all quartz Ti data were measured by EMPA at University of Oxford; see Matthews *et al.* (2012).

shards from the selected pumice samples was undertaken using VG Elemental PlasmaQuad PQII+ coupled to a frequency-quadrupled Spectron Systems Nd:YAG laser at the Institute of Geography and Earth Sciences, University of Wales, Aberystwyth. Analytical conditions were as follows: laser operating at 193 nm, low laser power (0·5–1 mJ, 5 Hz) to avoid shard shattering, a spot size of 10 or 20 μm, and landing the beam adjacent to EMPA spots. Ar was used as a carrier gas with an average gas flow of ~0·8 l min^{-1} and RF power of 1050–1080 W with Guard Electrode on. The laser was fired at 5 Hz, 10 J cm^{-2}, with a 10 s acquisition time and the Ar flow split through the sample chamber. Further details on operating conditions have been provided by Pearce *et al.* (2011). Si was used as an internal standard (Pearce *et al.*, 2002). Here, we use the SiO_2 contents of shards previously determined by EMPA (the specific value for each analysis was used, rather than an average). Concentrations of trace elements in the shard were then calculated by comparing the ratio of analyte signal intensity to internal standard intensity for the glass with the same ratio from a reference material. We used NIST SRM 610 glass as a reference material, taking major and trace element concentrations from Pearce *et al.* (1997). The calculated concentration in the glass was corrected for differences in the internal standard concentration between the unknown and reference material by multiplying by the ratio of SiO_2 wt % in the reference material to the SiO_2 wt % in the glass shard (Pearce *et al.*, 2002). Analyses were performed in two batches on the same day, and there were no differences in the range or means of data from each batch. Detection limits for many elements are in the 0·01–0·5 ppm range. In homogeneous materials LA-ICP-MS has a precision (reproducibility) of better than 10% at the 100 ppm level, and accuracy is typically better than ±10%. LA-ICP-MS instrumentation, calibration and analytical methods have been fully described by Perkins & Pearce (1995), Pearce *et al.* (1996, 1999, 2004, 2011) and Perkins *et al.* (1997).

Cathodoluminescence analysis

CL images were obtained using a panchromatic CL detector mounted on a JEOL electron microprobe at the University of Bristol, using a 22 nA beam current, 15 kV, and 42 s capture time, with image resolution of 1020 × 790 pixels (where 1 pixel is 3·5 μm). Quartz CL brightness is assumed to correlate with Ti concentration (and to a lesser extent with Al; Peppard *et al.*, 2001; Wark & Spear, 2005; Liu *et al.*, 2006*a*; Wark & Watson, 2006; Rusk *et al.*, 2008; Shane *et al.*, 2008*a*), suggesting that it is an important contributor to CL activation in magmatic quartz. Greyscale values of CL images can therefore be used as a proxy for Ti content, and continuous Ti profiles across all crystal zones can be interpolated from greyscale images calibrated by single EMPA Ti measurements. The correlation between greyscale and EMPA Ti concentrations used in the calibration is statistically significant, with R^2 values of 0·80–0·99 (although most data are at low and high Ti values, with few intermediate Ti concentrations). The CL greyscale profiles can therefore be used to provide a highly resolved (3 μm resolution) record of Ti uptake during quartz crystallization (e.g. Fig. 3).

Ti-in-quartz

With the discovery that temperature is the principal control on the Ti content of volcanic quartz (Wark & Spear, 2005), many studies have used the Ti content of quartz as a geothermometer (e.g. Wark & Watson, 2006; Wark *et al.*, 2007; Wiebe *et al.*, 2007; Shane *et al.*, 2008*a*; Smith *et al.*,

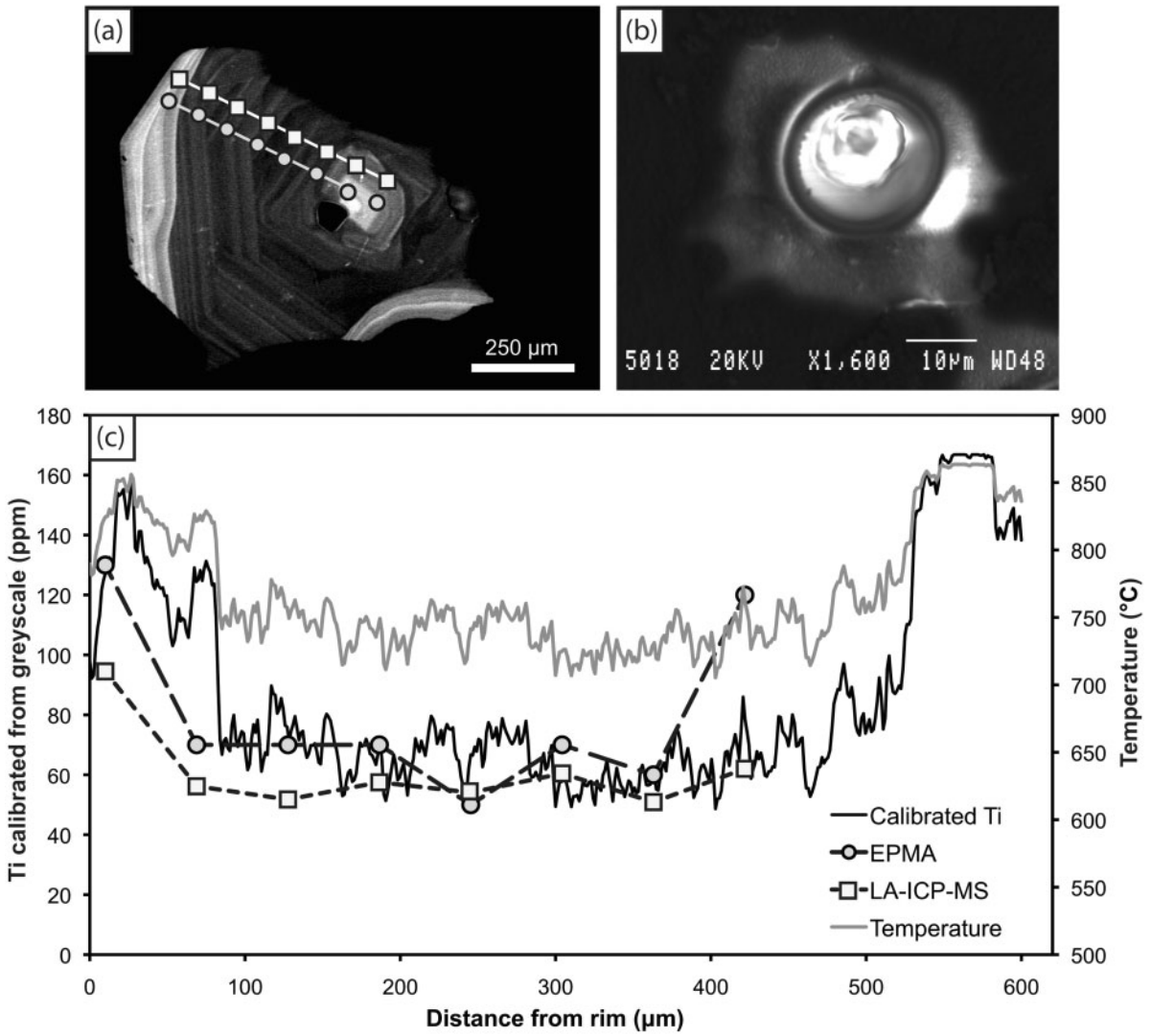

Fig. 3. Comparison of Ti-in-quartz analysis by EMPA, CL and LA-ICP-MS. (a) CL image of quartz crystal (Pl827-11) with position of Ti analysis transects by EMPA (circles) and LA-ICP-MS (squares); (b) SEM image showing detail of a single laser pit; (c) Ti concentrations from core to rim, with CL greyscale profile calibrated by EMPA data ('Calibrated Ti'), and corresponding TitaniQ temperature profile (grey line). Differences between analyses by EMPA and LA-ICP-MS on the extreme right spot in the quartz core are due to different zones in the quartz crystal being analyzed by the two techniques and not an error. The data strongly support that low CL is correlated with low Ti, and high CL with high Ti, although more data are required to prove that the high-frequency variations in CL are correlated directly with Ti.

2010). This is conventionally achieved by CL imaging of a crystal, and by assuming CL intensity is directly proportional to Ti content (Götze *et al.*, 2001; Wark & Spear, 2005). Electron microprobe analysis (EMPA) of the Ti content of discrete points along a core–rim profile allows use of the Ti-in-quartz, TitaniQ, geothermometer (Wark & Watson, 2006) to reconstruct quartz crystallization temperatures. Recent studies (e.g. Thomas *et al.*, 2010; Wilson *et al.*, in preparation) have, however, indicated that there may also be a significant pressure and compositional (X_{H2O}) effect on the Ti partitioning into quartz. Interpretations of temperature–pressure effects from the Ti-in-quartz method must therefore be made with caution, as we note in our application of it here.

EMPA and LA-ICP-MS

EMPA and LA-ICP-MS were used to establish the relationship between quartz growth features and CL and to allow use of the TitaniQ geothermometer (Wark & Watson, 2006; results discussed by Matthews *et al.*, 2012), as illustrated in Fig. 3. Ti concentrations in quartz were measured using a JEOL JXA-8800R electron microprobe at the Begbroke Science Park, University of Oxford, with a 15 kV accelerating voltage, 200 nA beam current and a beam

diameter of 10 μm. To obtain reliable Ti results at low abundance, Ti was analyzed on two spectrometers simultaneously, using count times of 800 s on the peak and backgrounds. Merging the Ti counts from the spectrometers resulted in low detection limits (<10 ppm) and low uncertainties (±11 ppm; 1SD) for Ti. The JEOL 8600 electron microprobe in the Research Laboratory for Archaeology and the History of Art, University of Oxford, was also used with a high beam current (100 nA), extended count times (900 s on peak and background), and a 10 μm beam diameter (which averages finer-scale CL zonation). Transects for Ti analyses were chosen on the basis of CL zoning, in particular targeting the core–rim interface. CL greyscale values were calibrated using discrete electron microprobe Ti analyses (Fig. 3). Electron microprobe analyses were spaced at 100 μm (av.) intervals (spacing ranged from 45 to 200 μm depending on crystal size) along core-to-rim profiles. Ti transects were obtained using LA-ICP-MS (as described above). These Ti concentrations from LA-ICP-MS correlate well with those obtained by EMPA (Fig. 3).

μ-*XRF and XANES*

Synchrotron μ-XRF mapping of Ti in quartz was performed at the Diamond Light Source Ltd (DLS) Microfocus X-ray Spectroscopy Beamline I18, Oxfordshire (Mosselmans *et al.*, 2008, 2009). Detailed description of beamline components, parameters and operating conditions can be found at http://www.diamond.ac.uk/Home/Beamlines/I18.html).

The small spot sizes and the counts generated using synchrotron μ-XRF are ideal for this study as high-resolution Ti maps spanning core to rim could be rapidly collected (2 s per analysis). The spatially resolved Ti concentrations from synchrotron μ-XRF allow us, for the first time, to accurately assess the relationship between CL intensity and Ti content, and obtain spatially resolved measured Ti concentrations to apply in the Ti-in-quartz geothermometer (Wark & Watson, 2006). High-resolution μ-XRF maps across the core–rim interface in the quartz (described below) display the complex Ti-zonation patterns seen in the CL images, and these can be directly modeled. One drawback with the synchrotron technique in our context is beam penetration into the crystal (compared with CL and EMPA, which are more shallow or surface dominated). Beam penetration depth was ~15 μm (see details of X-ray attenuation depth in Appendix B), which results in counts being effectively depth-averaged.

Selected crystals were mounted in epoxy discs and polished prior to μ-XRF mapping. The target areas for synchrotron Ti mapping were chosen to capture the chemical zoning of both the cores of quartz grains and their rims, and to accurately define the scale of the boundary zones between core and rim. Crystal transects were mapped at a high spatial resolution with analyses every 3 μm horizontally and 4 μm vertically. An analysis time of 2 s per spot allowed multiple Ti-transects to be analyzed per day of beam time. Acquisition time for a typical map, 500 μm long by 50 μm wide, was ~75 min. Quartz crystals from selected pumice samples from each eruption (Whakamaru, EQF, YTT) were analysed, chosen to provide the most representative suite of quartz grains that had been previously characterized in terms of their CL zonation, textural features, and Ti contents.

Ti maps were obtained by rastering a polished sample at 45° to the beam and tuning the beam to an incident energy of 5·5 keV. A nine-element Ortec monolithic Ge detector was used. The incident X-ray beamsize was ~3 μm by 4 μm. The μ-XRF spectra were fitted for Ti using the PyMCA package (Solé *et al.*, 2007) and the elemental distribution map was generated from the fitted spectra. The elemental maps show the distribution of Ti from core to rim of each quartz crystal as described below. Quantification of μ-XRF Ti intensity maps involved using a well-characterized homogeneous quartz crystal with 90 ppm Ti (analysed by EMPA). The Ti intensity was normalized to the scatter peak, which accounts for incident beam intensity, detector geometry and sample thickness, and to the Ti/scatter ratio from the standard. Precision on synchrotron Ti-in-quartz data is ±3 ppm, and the data compare well with CL-calibrated Ti data based on EMPA.

Titanium XANES spectra were also measured on beamline I18 at the Diamond Light Source Synchrotron, providing information on the local coordination environment of Ti ions in the same mapped quartz crystals (e.g. Waychunas, 1987). We compare these spectra with a universal standard, volcanic glass, magnetite, clinopyroxene and Ti-metal. Results are also described in comparison with results from experimentally grown quartz crystals from Thomas *et al.* (2010). Spectral data were normalized to account for differences in Ti concentrations between samples, detector and amplifier settings, using Athena software (Ravel & Newville, 2005).

TitaniQ

The Ti content of hydrothermally grown quartz has been empirically described as a function of both temperature (Wark & Watson, 2006) and pressure, with a ±1 kbar pressure change corresponding to ±20°C change in temperature and vice versa (Thomas *et al.*, 2010). The Ti content of quartz (Ti_{qtz}) was proposed by Wark & Watson (2006) to be related solely to temperature, using the equation

$$T = \frac{-3765}{\log(Ti_{qtz}/a_{TiO_2}) - 5{\cdot}69} \quad (1)$$

where T is temperature (K) and a_{TiO_2} is activity of Ti in the quartz. This geothermometer was calibrated experimentally by Wark & Watson (2006) by synthesizing

quartz in the presence of rutile and hydrous silicate melt, at temperatures of 600–1000°C and at 1·0 GPa.

None of the eruption deposits studied here contain rutile and therefore the activity of Ti in the melt (a_{TiO_2}) was estimated to allow use of the TitaniQ geothermometer. It was calculated for each eruption assuming ideal exchange equilibria between coexisting Fe–Ti oxides, and using the expanded method of Wark *et al.* (2007) and Reid *et al.* (2010). The exchange reaction

$$2FeTiO_3(\text{ilmenite}) = TiO_2(\text{rutile}) + Fe_2TiO_4(\text{ulvöspinel}) \quad (2)$$

was used, also accounting for non-ideality in the solid solutions, given by the following equations:

$$6TiO_2(\text{rutile}) + 2Fe_3O_4(\text{magnetite}) = 6FeTiO_3(\text{ilmenite}) + O_2 \quad (3)$$

$$3TiO_2(\text{rutile}) + 2Fe_3O_4(\text{magnetite}) = 3Fe_2TiO_4(\text{ulvöspinel}) + O_2. \quad (4)$$

Thermodynamic data from Holland & Powell (1998), solution models from White *et al.* (2002), and ilmenite–hematite solid solution ordering states from Ghiorso (1990) were then used to estimate a_{TiO_2}, using the eruption temperatures from Table 2. These eruption temperatures are calculated using the Ghiorso & Evans (2008) Fe–Ti oxide geothermometer. It should be noted that determination of a_{TiO_2} in the melt is critical for TitaniQ geothermometry. A full discussion of the issues with assuming a single value of a_{TiO_2} for entire zoned crystals has been provided by Matthews *et al.* (2012). The focus here is on the calculation of magmatic timescales, however, rather than the precise quantification of temperature fluctuations.

Table 2: Geothermobarometery data for eruptions

	Whakamaru	EQF	YTT
Fe–Ti oxide T (°C)	770 ± 46	745 ± 27	760 ± 16
log fO_2	−14·0 ± 1	−15·0 ± 0·8	−15·0 ± 0·6
Amphibole T (°C)	840 ± 50	768 ± 10	828 ± 3
Amphibole P (MPa)	125 ± 66	90 ± 9·5	168 ± 6
Depth (km)	4·7 ± 3	3·4 ± 0·4	6·4 ± 0·2

Fe–Ti oxide temperatures relate to eruption temperature, and use the Ghiorso & Evans (2008) geothermometer. Amphibole P, T and depth were calculated using the geothermometer of Ridolfi *et al.* (2010). YTT and EQF calculations were made using Fe–Ti oxide data and amphibole compositions reported by Chesner (1998) and Molloy *et al.* (2008). Whakamaru data (measured by EMPA at University of Oxford) and intensive parameters have been reported by Matthews *et al.* (2012).

The Ti concentration in quartz may also have a significant pressure dependence, as described by the equation

$$P\,(\text{kbar}) = \frac{(-a + bT + RT\ln a_{TiO_2} - RT\ln XQtz_{TiO_2})}{c} \quad (5)$$

where $a = 60952 \pm 3177$, $b = 1{\cdot}52 \pm 0{\cdot}39$, $c = 1741 \pm 63$, R is the universal gas constant (8·3145 J K^{-1}), T is temperature in K, and $XQtz_{TiO_2}$ is the mole fraction of TiO_2 in quartz (Thomas *et al.*, 2010). The parameters a, b and c have been established by a least-squares fit of experimental Ti-in-quartz solubilities (Thomas *et al.*, 2010). This proposed pressure dependence means that higher Ti contents can reflect higher temperatures, lower pressures, or a combination of the two effects. Ti partitioning and thus Ti contents in quartz may also be affected by compositional changes in the magma chamber (which affect the effective solubility of Ti in the melt). Therefore, interpretations of the nature of any changes in the intensive parameters (T, P, X_{H2O}) of the system based on changes in Ti-in-quartz must be made with caution (for full discussion see Thomas *et al.*, 2010; Matthews *et al.*, 2012; Wilson *et al.*, in preparation). This uncertainty does not, however, affect our interpretations of the pre-eruptive re-equilibration or diffusion timescales following such changes, as discussed below.

Diffusion methodology, calculation of diffusion timescales

Quartz crystals from all three eruptions display sharp gradients in Ti between the low-Ti core and high-Ti rims (see Results). To constrain the timescale between the growth of these rims and eruption we conduct diffusion modeling calculations as outlined below. Ti gradients along the high-resolution μ-XRF profiles, and corresponding calibrated CL greyscale profiles (with a resolution of 3 μm), provide the data for three independent diffusion modeling techniques. We describe these methods as: '1D', '1D corrected' and '2D Lattice Boltzmann' techniques as explained below.

Diffusion is modeled using quartz Ti diffusivities and activation energies from Cherniak *et al.* (2007). An activation energy (A_{Ea}) of 273 ± 12 kJ mol^{-1} was assumed for diffusion parallel to the c-axis in synthetic quartz and a Ti diffusion rate of $2{\cdot}7 \times 10^{-15}$ μm^2 s^{-1} at 770°C (Cherniak *et al.*, 2007). We assume that the quartz core–rim zone boundary (which marks the compositional step in Ti) was initially vertical. This assumption gives maximum timescales, and does not account for the possibility that Ti concentration was changing during crystal growth (which may account for the complex features observed in some of the Ti profiles). As there is only limited anisotropy in quartz-Ti diffusion it is not necessary to account for the orientation of the profile relative to the crystal (for comparison, Ti

diffusion normal to the *c*-axis in synthetic quartz is $2{\cdot}21 \times 10^{-21}\,m^2\,s^{-1}$ at 850°C; Cherniak *et al.*, 2007).

1D analytical diffusion technique

For 1D diffusion modeling we follow the approach of Morgan *et al.* (2004) and the method used by Wark *et al.* (2007). This method uses the width of Ti zone boundaries in quartz (as this is dependent on Ti diffusion rate under the ambient conditions), with the assumption that the major step in Ti content (and hence CL brightness) was initially vertical and related to the latest major event (Wark *et al.*, 2007). We use a step function to describe the initial concentration, where $C(x, t=0)$ is normalized to be either zero or unity on either side of the compositional step (core–rim boundary). The boundary at the edge of the quartz crystal was set to $C=1$ around the entire crystal. This choice of boundary condition does not affect the calculations, however, because the distance between the crystal boundary and the Ti-rich rim to Ti-poor core boundary is significantly greater than the diffusion length observed on measured profiles.

We use an A_{Ea} of $273\,kJ\,mol^{-1}$; diffusivity (D_o) of $7 \times 10^{-8}\,m^2\,s^{-1}$, gas constant ($R$) of $8{\cdot}3145\,J\,K^{-1}$, and temperatures of 770°C (Whakamaru), 760°C (YTT), and 745°C (EQF), to calculate time (t, in s) (see Supplementary Data 3). The eruption temperatures are derived from Fe–Ti oxides, calculated using the geothermometer of Ghiorso & Evans (2008) (Table 2). Titanium diffusivity (D_{Ti}, in $m^2\,s^{-1}$) at a temperature (T, K) is given by the equation

$$D_{Ti} = D_o \exp\left(\frac{A_{Ea}}{RT}\right) \tag{6}$$

[for diffusion parallel to (001) in quartz; Cherniak *et al.*, 2007]. The diffusion timescale (t) can be obtained from the equation

$$C = \frac{1}{2}\,\mathrm{erfc}\left(\frac{x}{2\sqrt{D_{Ti}t}}\right) \tag{7}$$

(Morgan *et al.*, 2004), where C is the normalized Ti concentration, D_{Ti} is the Ti diffusivity ($m^2\,s^{-1}$), t is the diffusion time, and x is the position measured in microns along the profile and centered on the step (the maximum extent of diffusion at the half-width). The best-fit solutions to equation (7) were determined by modeling Ti-compositional profiles for different timescales and, by visual inspection, choosing the profile that most closely matched the gradient of the measured greyscale-calibrated Ti profile.

1D analytical corrected technique

In the 1D analytical technique we assume that the concentration profiles of Ti can be modeled with a 1D diffusion equation, but with refinement by incorporation of the angle of the profile with respect to the direction perpendicular to the diffusion boundary. In this method, diffusion from an initially vertical step in concentration is given by equation (7) as above. In an ideal situation, the measurement of Ti concentration at distance Δx from the step midpoint (where the midpoint concentration, $C_m = 0{\cdot}5$) allows calculation of time, t, for Ti diffusion in a quartz crystal [as derived from equation (7)]:

$$t = \frac{\Delta x^2}{4D_{Ti}\,[\mathrm{inverfc}(2C)]^2}. \tag{8}$$

In equation (8), inverfc is the inverse complementary error function; C the normalized concentration measurement, and Δx its distance from the midpoint of the compositional step. The angle (α) between the measured concentration profile and the core–rim boundary compositional gradient can be accounted for by rescaling Δx with $\Delta x \cos\alpha$, as described in Appendix A. The effect of the angle correction has also been reported by Costa & Morgan (2010). The method of Morgan *et al.* (2004) addressed the crystal orientation issue by carefully mounting crystals to control the sectioning angle.

In reality, the actual concentration profiles display complex features that cannot be attributed to 1D diffusion, such as 2D effects and local heterogeneities, in addition to analytical errors in the Ti measurements. We therefore expect that, when applying equation (8) for the few measurements in the vicinity of the step midpoint, the times obtained may differ substantially owing to these complications (the 1D method has the same limitations). The times obtained by the 1D techniques are, however, useful in providing an estimate of the diffusion time, an average time calculated for each profile, and an assessment of the quality of the data to be fitted in the diffusion modeling calculations. This approach also offers simple diagnostics when diffusion times calculated for each point show a large variability (e.g. an asymmetric diffusion profile), which would indicate local heterogeneities associated with structural effects (e.g. associated with single defects), error in the concentration measurements, or complex pre-diffusion concentration profiles.

2D Lattice Boltzmann modeling

To overcome the above shortcomings, we use a model based on the Lattice Boltzmann (LB) method to solve for diffusion in two dimensions (Huber *et al.*, 2008, 2010*a*, 2012*a*), which allows us to account for complex geometries in the physical boundaries of crystals. In the LB method, the diffusion equation incorporates the evolution of particle distribution functions described by simple kinetic rules that allow us to recover the correct dynamics (diffusion) with isotropic or anisotropic diffusion coefficients.

Initial calculations are computed in dimensionless time using a Fourier number (Fo), which is defined as

$$\mathrm{Fo} = \frac{D_{\mathrm{Ti}} t}{L^2} \tag{9}$$

where D_{Ti} is the diffusivity of Ti, t is the duration of the diffusion event, and L is the length-scale of interest (the distance in microns over the compositional change). In isotropic conditions, the Fo number fully characterizes the state of the system and allows us to normalize the space–time relationship of the diffusion equation, and thus solve for time.

The evolution of the particle distribution functions is described by a discretized version of Boltzmann's equation with a simplified collision operator (Bhatnagar *et al.*, 1954; Huber *et al.*, 2011),

$$f_i(x+v_i\mathrm{d}t, v_i, t+\mathrm{d}t) - f_i(x, v_i, t) = \omega[f_i^{\mathrm{eq}}(x, v_i, t) - f_i(x, v_i, t)] \tag{10}$$

where f_i is the distribution function for particles moving along the velocity vector connecting two neighbor nodes v_i, x is the position on the lattice, and $1/\omega$ is the relaxation time towards an equilibrium described by f_i^{eq}. The diffusion coefficient is related to ω according to the equation

$$D_{\mathrm{Ti}} = c_s^2 \mathrm{d}t\left(\frac{1}{\omega} - \frac{1}{2}\right) \tag{11}$$

where c_s^2 is the sound speed of the lattice, which depends on the lattice topology [for further details of derivation, see Huber *et al.* (2011)]. The equilibrium distribution f_i^{eq} is given by

$$f_i^{\mathrm{eq}}(x, v_i, t) = w_i C(x, v_i, t) \tag{12}$$

where w_i are the lattice weights. The local concentration is the sum of the distributions, given by

$$C = \sum_{i=0}^{4} f_i = \sum_{i=0}^{4} f_i^{\mathrm{eq}}. \tag{13}$$

Through a Chapman–Enskog expansion, the set of equations (10)–(13) retrieves a 2D diffusion equation where the diffusivity is defined by equation (11) (Wolf-Gladrow, 2000). We use the newly developed algorithm by Huber *et al.* (2012*a*) that allows the boundary concentration along the crystal interface to be fixed. Further information on the diffusion model derivation has been given by Chopard & Droz (1998) and Huber *et al.* (2012*a*).

The modeling uses an area of each crystal as an input, or the entire crystal, and the best fit is found by comparing a modeled line segment with the real data. Using the modeled elemental gradient, which displays the best fit to the real data, we calculate a timescale for diffusion from the Fourier number. Using the Arrhenius relation for Ti diffusion parallel to (001) in quartz,

$$D_{\mathrm{Ti}} = 7 \times 10^{-8} \exp(-273 \pm 12\ \mathrm{kJ\ mol^{-1}}/RT)\ \mathrm{m^2\ s^{-1}} \tag{14}$$

we are able to estimate the time period for diffusion at any temperature. Diffusion times are quoted at an eruption temperature, calculated from Fe–Ti oxides (see Results and Table 2). The angle of the core–rim interface at depth (β) is accounted for by rescaling diffusion results (time) by $\sin^2\beta$ (see below and Table 3).

Stirring and reactivation timescales

To extend the record of magma chamber processes derived from quartz, we also calculate timescales of stirring of the rhyolitic chamber (defined as the time required to homogenize the convecting magma body) and mush reactivation (the period between the onset of mafic intrusion and the time at which the crystal mush is unlocked and open to whole-chamber convection; Huber *et al.*, 2010*b*).

The stirring timescale (τ_{m}) is calculated for the Whakamaru magma reservoir assuming steady-state convection, using

$$\tau_{\mathrm{m}} = \frac{1}{2\dot{\varepsilon}} \ln\left(\frac{\dot{\varepsilon} H^2}{\kappa}\right) \tag{15}$$

from Huber *et al.* (2009) where 5–10 overturns in the chamber is the criterion for a stirred chamber, $\dot{\varepsilon}$ is the shear strain induced by convective stirring, H is the magma chamber thickness, κ is the thermal diffusivity ($10^{-6}\ \mathrm{m^2\ s^{-1}}$; Turcotte & Schubert, 2002; Huber *et al.*, 2010*b*, 2012*b*), and H^2/κ is the diffusion timescale of interest in the mixing process (Table 4).

The average strain rate depends on the Rayleigh number (Ra: ratio of diffusive to advective timescales for heat transfer), which for large magma bodies is $>10^9$ (Coltice & Schmalzl, 2006). The Rayleigh number is given as

$$\mathrm{Ra} = \frac{\Delta\rho g H^3}{\kappa\mu} \tag{16}$$

where $\Delta\rho$ is the difference in density that drives convection, g is the gravitational constant, and μ is the viscosity of the melt (10^5 Pa s; Scaillet *et al.*, 1998; Cottrell *et al.*, 1999; Bachmann & Bergantz, 2006). Strain rate is calculated using

$$\dot{\varepsilon} = 0 \cdot 023\left(\frac{\kappa}{H^2}\right)\mathrm{Ra}^{0\cdot 685} \tag{17}$$

for $10^3 \leq \mathrm{Ra} \leq 10^9$ (Coltice & Schmalzl, 2006; Huber *et al.*, 2009). Alternatively, this calculation can be modified, using boundary-layer theory, to

$$\dot{\varepsilon}_{\mathrm{BL}} = 0{\cdot}271\left(\frac{\kappa}{H^2}\right)\mathrm{Ra}^{2/3} \tag{18}$$

Table 3: Comparison of times (in years) for diffusion across quartz core–rim boundary for Whakamaru, Toba (YTT) and Earthquake Flat quartz, using both 1D and 2D diffusion methods applied to CL data

Crystal	1D methods				2D LB from CL greyscale					
	Angle α	1D (years)	Corrected 1D av. (years)	Uncertainty (± years)	Angle β	Fo	2D (years)	New Fo	2D (years) with angle	Uncertainty (± years)
Whakamaru quartz, at 770°C										
P1910-15	8	250	245	30	35	2·5	210	0·7	60	30
P1910-18	5	200	200	50	35	1·0	152	0·3	45	15
P1910-19	10	150	145	30	50	1·0	100	0·9	55	40
P1910-22	5	100	100	20	60	0·5	45	0·4	35	15
P1910-20	0*	50, 150	100	100	55	1·1	110	0·6	60	30
P1915-22	20	50	45	10	25	0·8	120	0·2	25	10
P1920-24	40	150	90	40	70	0·5	32	0·5	30	20
P1920-26	40	100	60	20	50	4·0	45	2·1	*25*	10
P1827-7	30	100	75	15	60	0·3	11	0·7	10	10
P1827-22	15	25	20	5	80	0·5	10	0·5	10	5
P1905-11	5	30	30	20	45	0·8	130	0·4	60	25
P1905-12	45	300	150	25	90	0·3	45	0·3	45	25
P1905-17	20	130	115	15	40	1·5	35	0·6	15	10
P1905-23	0	60	60	10	80	0·5	45	0·5	45	15
P1905-19	15	60	55	35	55	1·0	*90*	0·7	*60*	30
Average		120	100						40	
Median		100	80						45	
Toba YTT quartz, at 760°C										
YTT-34	45	450	225	50	50	2·0	445	1·1	245	80
YTT-11	40	100	60	25	60	1·0	80	0·8	60	30
YTT-5	0	100	100	30	50	1·4	145	0·8	80	35
YTT-21	45	100	50	20	50	1·0	75	0·6	50	25
YTT-17	50	100	40	20	30	1·2	120	0·8	60	30
YTT-6	30	400	300	60	25	5·0	*2550*	0·9	200	70
Average		210	130						115	
Median		100	80						70	
Earthquake Flat quartz, at 745°C										
EQF-CL21	0	1000	1000	100	60	25·0	*3150*	19·5	*2450*	560
EQF-CL5	30	10	8	5	35	1·0	70	0·4	25	10
EQF-CL1	35	100	60	20	60	1·0	180	0·8	140	50
EQF-CL8	40	50	30	10	85	1·0	45	1·0	45	30
EQF-CL14	20	10	10	5	40	1·0	95	0·4	40	20
Average		235	220						540	
Median		50	30						45	

The 1D and 2D diffusion modeling is based on CL greyscale as a proxy for Ti content in quartz for core–rim boundaries of selected quartz crystals from each eruption. The angle (α) of the transect perpendicular to the boundary is incorporated in the analytical 1D approach (using $x\cos\alpha$ as explained in Appendix A). LB 2D diffusion modeling considers the angle (β) of the core–rim interface to the horizontal, as calculated using CL greyscale (see Fig. 8), where Fo is the Fourier number used in diffusion equations. Anomalously long times are indicated in italics and omitted from the average calculations. Overall uncertainty (± years) is attributed to curve fitting and temperature estimates (based ±10°C variation), calculated as the quadratically combined total.
*0° angle indicates a profile along a corner.

Table 4: Parameters and symbols used in thermodynamic calculations for silicic melts and a mafic intrusion

Thermodynamic parameter	Symbol	Value	Units
Density of intrusion	ρ_i	2900	$kg\,m^{-3}$
Density of mush	ρ_m	2400	$kg\,m^{-3}$
Difference in density that drives convection	$\Delta\rho$	10–100	$kg\,m^{-3}$
Thermal diffusivity	κ	10^{-6}	$m^2\,s^{-1}$
Viscosity of melt	μ	10^5	Pa s
Chamber volume	V	1000	Km^3
Chamber (mush) thickness (volume/surface area)	H	1	Km
Intrusion thickness	H_i	1	Km
Magma chamber depth	D	5	Km
Acceleration due to gravity	g	9·81	$m^2\,s^{-1}$
Shear strain (induced by convective stirring)	$\dot{\varepsilon}$		

Value for density of intrusion is taken from Cottrell *et al.* (1999) and Wark *et al.* (2007); density of mush from Blake & Ivey (1986) and Tait *et al.* (1989); viscosity from Scaillet *et al.* (1998), Cottrell *et al.* (1999) and Bachmann & Bergantz (2006); Whakamaru magma chamber volume estimate from Brown *et al.* (1998).

(Turcotte & Schubert, 2002; Huber *et al.*, 2009). In these calculations we use a density difference of $500\,kg\,m^{-3}$ between the mafic intrusion and the silicic crystal mush (using values from Blake & Ivey, 1986; Tait *et al.*, 1989; Wark *et al.*, 2007).

The reactivation timescale is defined as the period between the injection of mafic magma under a large crystal-rich reservoir and the time at which the crystal-mush is capable of undergoing whole-chamber convection (Huber *et al.*, 2012). This depends on the size and crystallinity of the magma, the size and frequency of magma intrusion carrying the enthalpy required to induce convection, and also the tectonic setting (in terms of phase assemblage and volatile contents of the crystal mush and the recharge magma; Huber *et al.*, 2010*b*, 2010*c*). The reactivation timescale is calculated using the equation

$$t_{react} = \frac{H}{\delta c^2}\left(\frac{\kappa\mu \mathrm{Ra}_{cr}}{\Delta\rho g}\right)^{2/3} \quad (19)$$

where κ is the thermal diffusivity, μ is the dynamic viscosity of the magma, $\Delta\rho$ is the density contrast responsible for the convective motions, H is the thickness of the magma body, and δ is the boundary layer thickness of the convecting magma (Huber *et al.*, 2012). Ra_{cr} is the critical Rayleigh number at which convection starts (of the order of 10^3). The constant $c \sim 4\,m\,a^{-1/2}$ was determined from the calculations of Huber *et al.* (2010*c*).

RESULTS

Eruption temperatures and glass chemistry

Eruption temperatures for the three eruptions were estimated using the Ghiorso & Evans (2008) Fe–Ti oxide geothermometer and compared with the Ridolfi *et al.* (2010) amphibole geothermobarometer. Published compositional data were used for these new geothermometers, with YTT data from Chesner (1998) and Liu *et al.* (2006*b*), EQF compositions from Molloy *et al.* (2008), and the Whakamaru dataset presented by Matthews *et al.* (2012). The average eruption temperatures used in the diffusion modeling are 770°C for Whakamaru, 745°C for EQF, and 760°C for YTT (see Table 2). All three eruptions are characterized by high-silica rhyolite magma (glass shards contain 77–78 wt % SiO_2, and $Na_2O + K_2O$ of 7·9–8·6 wt %; quoted anhydrous). Summary major and trace element glass chemistry for the eruption units is presented in Table 5.

Quartz characteristics

Quartz forms 20–40% of the crystal fraction in the Whakamaru pumices and characteristically occurs as coarse (<12 mm diameter), subhedral to anhedral crystals with resorbed rims (Fig. 4), indicating that they were in disequilibrium in their host melt prior to eruption. Quartz crystals are strongly zoned (Figs 3 and 4; see also Matthews *et al.*, 2012), with EMPA Ti concentrations ranging from 50 to 230 ppm (1SD uncertainties are ±1–2 ppm, which equates to ±1–3°C; the full dataset is provided in Supplementary Data 1), implying crystallization temperatures of 726–939°C [using the TitaniQ formulation, an activity of Ti in the melt given by $a_{TiO_2} = 0{\cdot}5$–0·6, and assuming no pressure dependence; Table 1; note the issues associated with pressure—refer to Thomas *et al.* (2010) and Matthews *et al.* (2012)]. Under CL all Whakamaru quartz grains show similar features: dark cores (low-Ti; 50–90 ppm) and an abrupt Ti concentration increase associated with a bright-CL rim (high-Ti; 150–230 ppm; see example in Fig. 3).

EQF and YTT quartz crystals display simpler zoning patterns. EQF quartz crystals are also characterized by bright-CL rims and dark-CL cores, with subtle oscillations in CL greyscale (Fig. 5). EQF quartz phenocrysts have a 1·5 mm maximum diameter and are anhedral with numerous internal resorption horizons observed in CL images. Resorption horizons tend to be associated with Ti-rich (bright-CL) zones, occurring either at the rim or midway along the crystal profiles. Ti in EQF quartz ranges from 41 to 133 ppm (Smith *et al.*, 2010; see Supplementary Data 1), with corresponding TitaniQ temperatures of 750–915°C [Table 1; assuming constant a_{TiO_2} of 0·4 calculated using Fe–Ti oxide data from Molloy *et al.* (2008)].

Similar to Whakamaru quartz, YTT quartz is also characterized by resorption and is highly fractured, most

Table 5: Average matrix glass compositions for selected Whakamaru, EQF and YTT pumices

	Whakamaru and Rangitaiki pumice samples												Earthquake Flat		Toba	
	P1905		P1910		P1915		P1827		P1920		SB1119		EQF11		YTT7	
	Ra		Ra		Ra		Wh		Wh		Wh					
EMPA (wt %)	(*n* = 33)	1SD	(*n* = 24)	1SD	(*n* = 26)	1SD	(*n* = 16)	1SD	(*n* = 20)	1SD	(*n* = 16)	1SD	(*n* = 6)	1SD	(*n* = 16)	1SD
SiO_2	77·22	0·25	77·77	0·21	77·27	0·67	78·32	0·42	77·39	0·20	77·86	0·25	76·89	1·02	77·66	0·28
TiO_2	0·14	0·02	0·14	0·02	0·17	0·03	0·10	0·02	0·14	0·01	0·06	0·02	0·10	0·00	0·08	0·03
Al_2O_3	12·50	0·16	12·47	0·13	12·41	0·50	12·49	0·27	12·71	0·14	12·77	0·21	12·43	0·19	12·74	0·12
FeO	0·92	0·16	0·81	0·18	1·19	0·17	0·30	0·08	0·63	0·24	0·33	0·08	0·96	0·09	–	–
MnO	0·03	0·02	0·04	0·02	0·04	0·03	0·03	0·03	0·02	0·02	0·03	0·02	0·05	0·02	0·07	0·06
MgO	0·12	0·01	0·10	0·02	0·19	0·05	0·02	0·02	0·07	0·03	0·02	0·01	0·10	0·01	0·07	0·02
CaO	0·51	0·18	0·62	0·06	0·84	0·08	0·69	0·14	0·75	0·06	0·58	0·04	0·76	0·03	0·90	0·12
Na_2O	2·54	0·47	2·65	0·22	2·54	0·13	3·24	0·56	3·32	0·14	3·34	0·23	3·72	0·09	3·15	0·15
K_2O	6·03	0·74	5·40	0·31	5·34	0·14	4·81	0·85	4·96	0·26	5·01	0·14	4·16	0·10	5·16	0·20
Total	95·81	0·79	95·91	0·88	95·83	1·10	96·05	1·65	95·92	1·26	95·85	1·22	99·20	1·21	95·97	0·54
LA-ICP-MS (ppm)	(*n* = 20)	1SD	(*n* = 24)	1SD			(*n* = 11)	1SD	(*n* = 22)	1SD	(*n* = 18)	1SD	(*n* = 6)	1SD	(*n* = 4)	1SD
Rb	207	37	194	35			176	25	166	13	173	14	122	6	252	63
Sr	28	28	36	19			60	8	65	8	16	8	42	1	39	28
Y	26	4	25	3			23	5	27	3	29	3	14	0	40	12
Zr	139	14	141	17			124	23	148	16	83	10	79	1	84	9
Nb	8	1	9	1			9	2	9	1	9	1	8	0	17	4
Cs	8	1	11	3			8	2	8	1	9	1	7	0	11	4
Ba	912	103	961	106			1093	148	1039	94	369	58	771	16	332	325
La	29	2	29	4			28	4	34	14	34	3	22	0	33	14
Ce	55	5	55	8			52	8	58	10	64	4	42	1	62	20
Pr	6	1	6	1			6	1	6	1	7	3	4	0	7	2
Nd	22	2	22	3			20	4	24	3	27	3	15	2	25	6
Sm	5	1	4	1			4	2	5	2	6	2	2	0	5	1
Eu	0	0	0	1			0	0	0	0	0	0	1	1	0	0
Gd	5	1	5	2			4	1	5	1	5	1	2	0	5	1
Tb	1	0	1	0			1	0	1	0	1	0	0	0	1	0
Dy	4	1	5	1			4	1	5	1	6	1	3	0	6	2
Ho	1	0	1	0			1	0	1	0	1	0	1	0	1	0
Er	4	1	3	1			3	0	3	1	4	1	–	–	4	1
Tm	1	0	1	0			1	0	0	0	1	0	–	–	1	0
Yb	3	1	3	1			3	1	4	1	4	1	–	–	5	2
Lu	1	0	1	0			0	0	1	0	1	0	–	–	1	0
Hf	5	1	5	1			5	1	5	1	4	1	3	0	3	0
Ta	1	0	1	0			1	0	1	0	1	0	–	–	2	1
Pb	30	47	28	10			20	4	15	2	20	3	–	–	35	6
Th	20	2	21	3			18	3	22	3	25	2	11	1	32	7
U	4	1	4	1			5	1	4	0	5	0	3	0	5	2

Sample units are as follows: Ra, Rangitaiki; Wh, Whakamaru. Major element data were obtained by EMPA; trace element data by LA-ICP-MS analysis. Numbers are quoted as averages of *n* analyses, with 1 standard deviation (1SD). EMPA major element and SIMS trace element EQF data are from Smith *et al*. (2010); YTT trace element data are from Chesner & Luhr (2010).

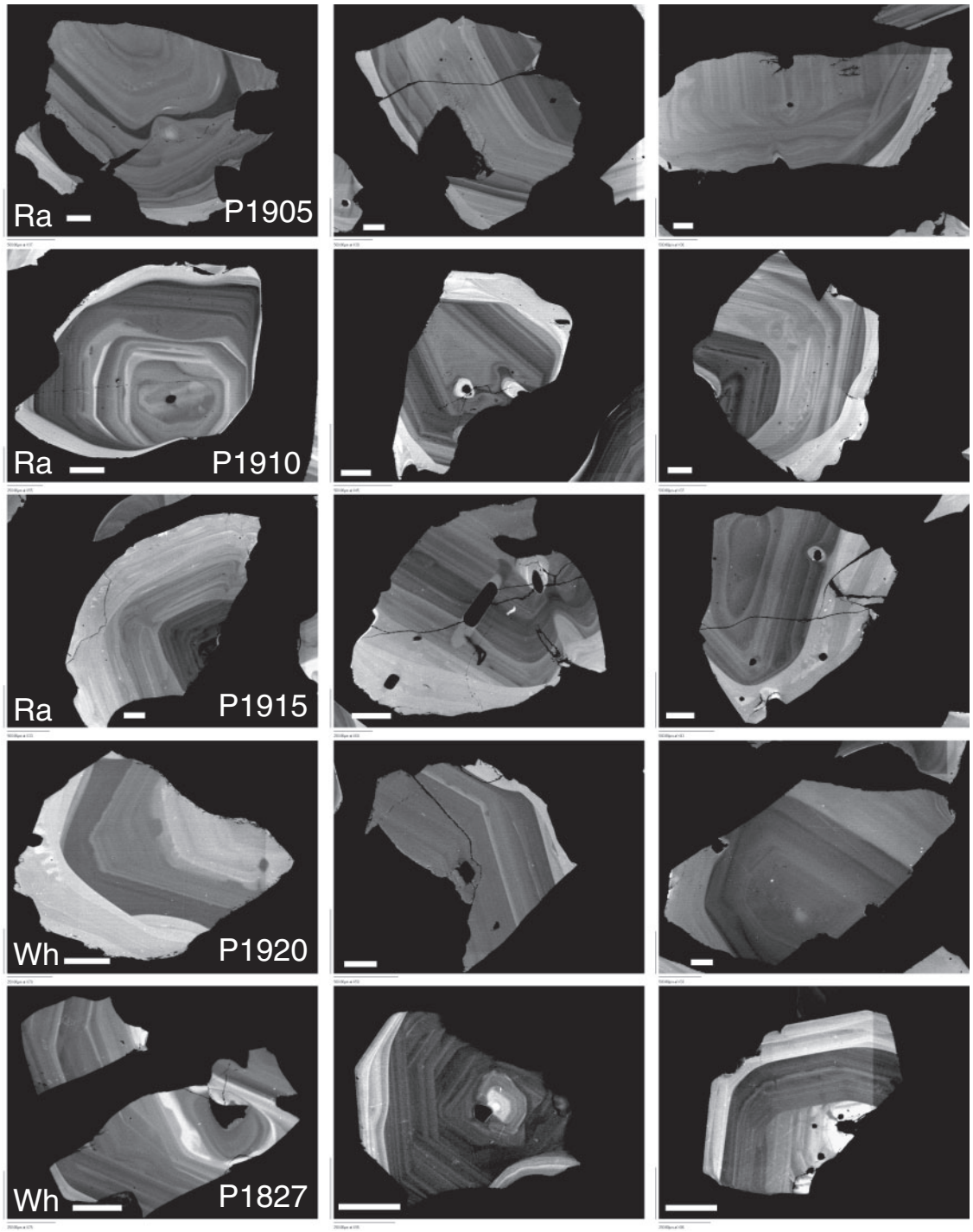

Fig. 4. CL images of selected quartz crystals. Scale bar represents 250 μm. Wh, Whakamaru quartz; Ra, Rangitaiki quartz. Sample codes: P1905, P1910 and P1915 are basal Rangitaiki pumices; P1920 and P1827 are Whakamaru. Note that the bright-CL rims on many of the crystals (up to 250 μm wide) occur after a significant resorption horizon. For further discussion see Matthews *et al.* (2012).

probably as a result of quenching and bursting of over-pressurized melt inclusions during pre-eruptive overheating and/or decompression, and syn-eruptive shattering (Tait, 1992; Best & Christensen, 1997; Gualda *et al.*, 2004; Bindeman, 2005). YTT quartz CL zoning displays both reverse and normal patterns and broad zones of homogeneous CL, however (Fig. 6). All YTT quartz crystals are characterized by an abrupt Ti compositional step near the

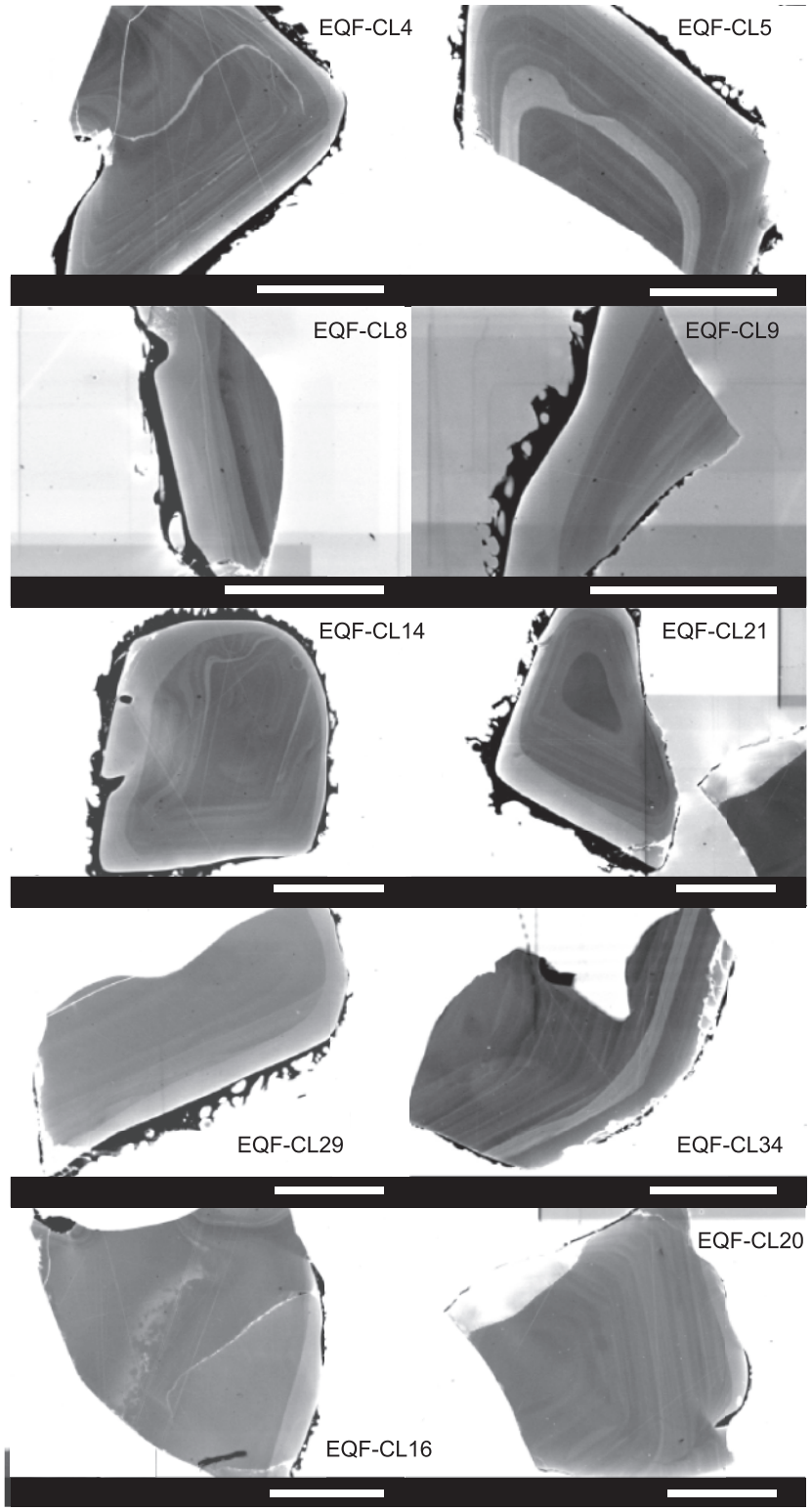

Fig. 5. Selected CL images of Earthquake Flat (EQF) quartz crystals [modified from Smith *et al.* (2010)]; zoning is less complex with some bright-CL rims and internal bright zones. Scale bar is 500 um for all images.

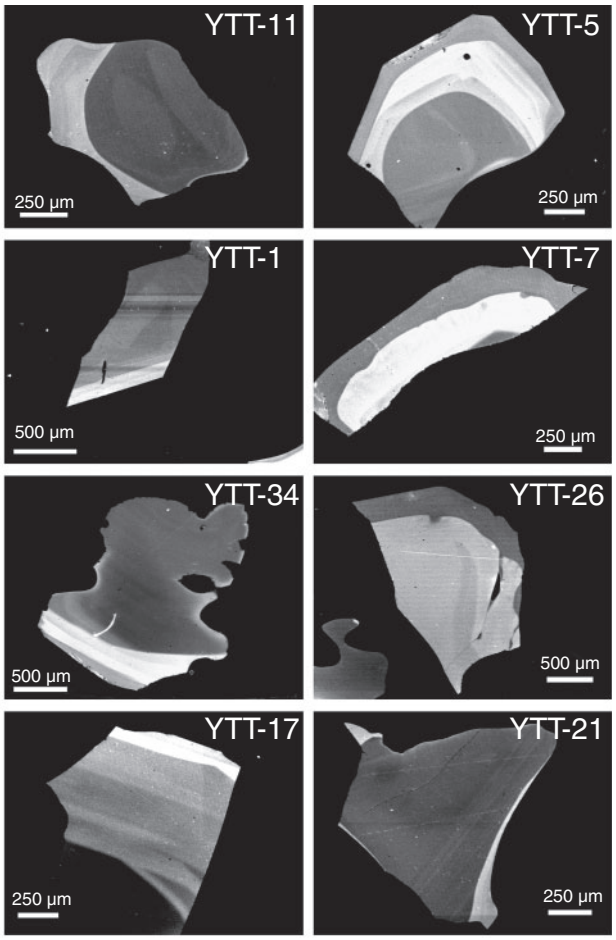

Fig. 6. CL images of selected YTT (Toba) quartz crystals (note that very little fine-scale zoning is evident).

crystal rim, which is diffusion modeled. Ti in YTT quartz ranges from below detection limit (10 ppm) to 214 ppm (Supplementary Data 1), which corresponds to temperatures of <594–958°C (Table 1; assuming constant a_{TiO_2} of 0·5 calculated using Fe–Ti oxide data from Chesner (1998) and consistent with calculations of Gaither *et al.*, 2009).

Ti-in-quartz μ-XRF maps

We observe a strong correlation between CL greyscale values and μ-XRF measurements of Ti concentration in quartz (Figs 7–9). Quartz zonation patterns indicated by the two techniques also compare well, with both the CL and synchrotron profiles showing high-Ti rims and low-Ti cores for Whakamaru and YTT quartz (Figs 7 and 8). The two profiles are offset owing to CL being a surface measurement (e.g. a 15 keV beam would penetrate a maximum of ~2·5 μm into quartz, with 70% of the signal coming from depths of less than 1·25 μm; Stevens-Kalceff, 2009) and μ-XRF incurring an angle of penetration effect as described above (Figs 7 and 8). This offset (in addition to a 'blurring' effect owing to depth-averaging) allows calculation of the angle of the core–rim boundary with respect to the analysis surface (Fig. 10). Because of the averaging effect caused by μ-XRF beam penetration (Fig. 10) a combination of CL and μ-XRF data is used here for diffusion modeling to provide upper and lower constraints on the diffusion time (Figs 11 and 12).

X-ray absorption near-edge structure

XANES spectra provide information on the Ti coordination environment in quartz and allow us to investigate the possible mechanisms by which Ti enters the quartz structure. XANES spectra were collected from Whakamaru quartz and reference materials including EQF matrix glass, clinopyroxene (Minoan and Afar basalt), magnetite (Afar, Ethiopia) and Ti foil (see Supplementary Data 2). We compare our XANES spectra (particularly focusing on the Ti pre-K-edge absorption peak) with experimental results from Thomas *et al.* (2010), and with previously characterized materials that contain Ti in different coordination positions. The pre-edge feature in spectra of quartz crystals most notably consisted of a single peak at ~4969 eV that is more intense and at lower energies than the multiple pre-edge features observed for rutile (Waychunas, 1987; Thomas *et al.*, 2010). No significant changes in spectra were observed for different Ti concentrations (and corresponding temperature–pressure conditions recorded by core vs rim), suggesting that the Ti (concentrations <200 ppm) always sits within the same position within these volcanic quartz crystals. This is consistent with the findings of Thomas *et al.* (2010). Results are provided in Supplementary Data 2.

Diffusion timescales

The presence of abrupt zoning (Ti compositional steps occurring over <30 μm) in the CL and Ti profiles in all the analyzed quartz crystals suggests short crystal residence times in the source magma chamber(s). If residence times were sufficiently long after formation of the abrupt compositional step, this would have resulted in a progressively smoother zoning profile until a linear core-to-rim profile was produced (Zellmer *et al.*, 1999; Costa & Chakraborty, 2004; Morgan & Blake, 2006; Wark *et al.*, 2007). It is thus possible to determine the maximum time elapsed between the growth of crystal rims and eruption by using the diffusion methods outlined above for Ti in quartz. The three methods for examining diffusion across the significant core–rim crystal boundary are utilized here to constrain the time required to generate the observed elemental gradient (as outlined in the Methods section). We focus on the core–rim interface (using data from both CL greyscale and μ-XRF) to determine the timescales associated with the last significant compositional event recorded by quartz. Results are presented in Table 3, which shows differences in diffusion timescales for

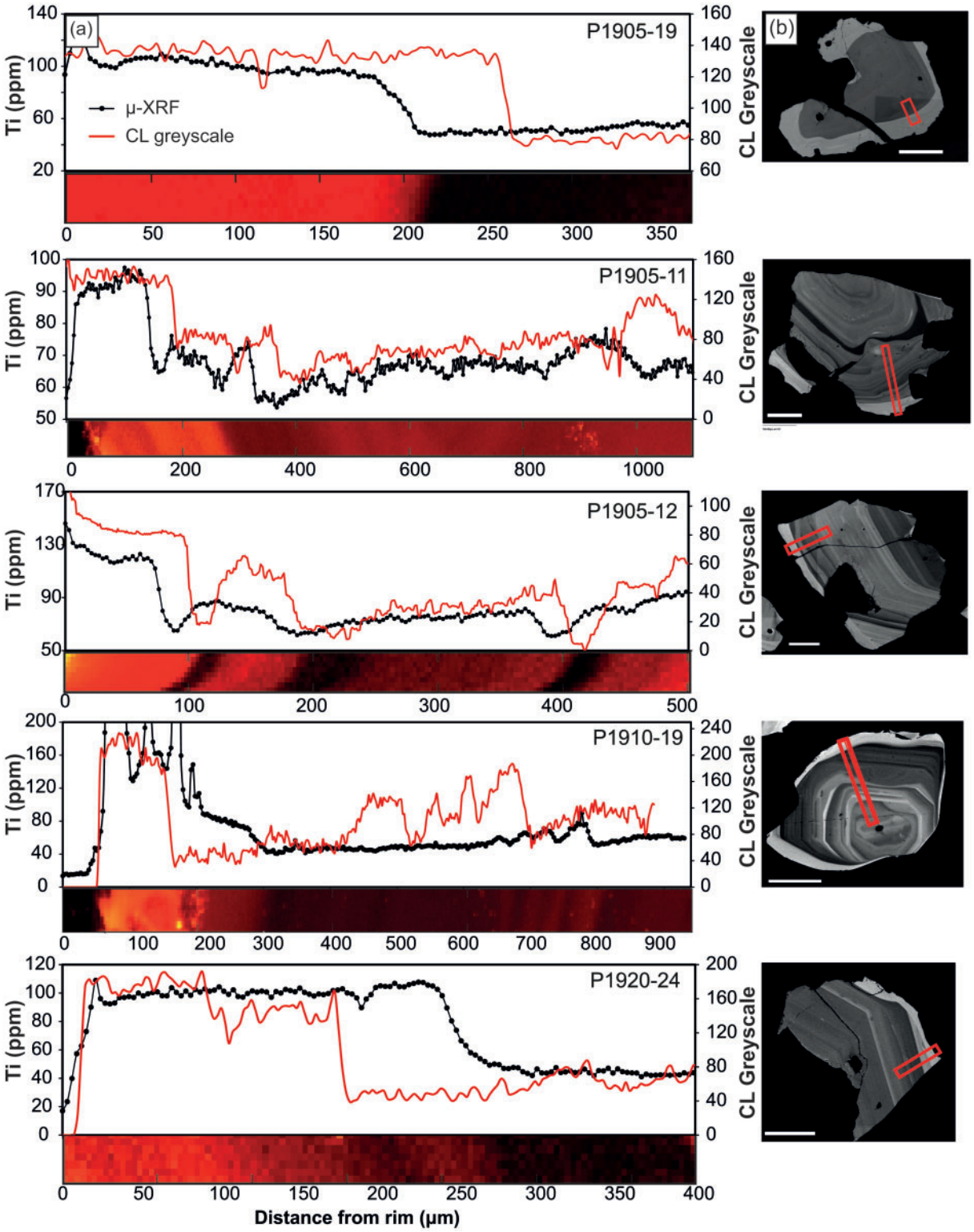

Fig. 7. (a) Synchrotron Ti maps of Whakamaru quartz plotted against Ti (ppm) transects (black) with CL greyscale transect (red) for comparison. Intensity of the colour relates to Ti content, where bright reds and yellows indicate high Ti, and black records very low Ti values. The sharp interface between high-Ti (bright-CL) crystal rims and low-Ti (dark-CL) cores should be noted. Some of the high-frequency variation in CL is not seen in the μ-XRF Ti profile. The μ-XRF maps (at the bottom of each Ti profile) have a 3 μm × 4 μm pixel size. (b) CL images of quartz crystals with zone of transect marked by red rectangle; scale bar represents 500 μm.

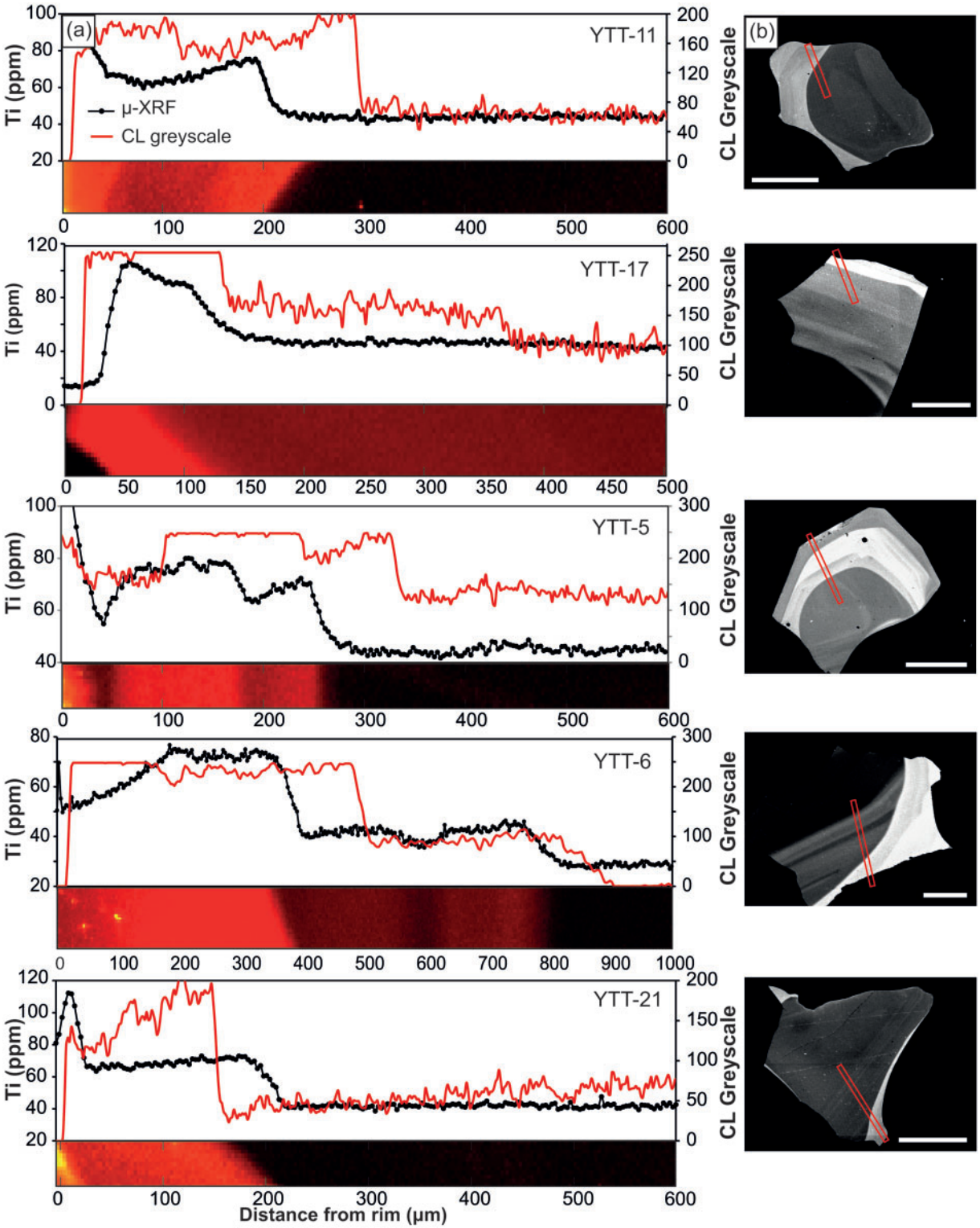

Fig. 8. (a) Synchrotron Ti maps of YTT quartz plotted against Ti (ppm) transects (black) with CL greyscale transect (red) for comparison. The sharp interface between high-Ti (bright-CL) crystal rims and low-Ti (dark-CL) cores should be noted. Most YTT quartz are characterized by high-Ti rims of various thickness, but some (e.g. YTT-5) have reverse-zoned patterns. The u-XRF maps (at the bottom of each Ti profile) have a 3 μm × 4 μm pixel size. Intensity of the colour relates to Ti content, where bright reds and yellows indicate high Ti, and black records very low Ti values. High-Ti recorded at rim in the synchrotron transects is due to adhering glass. (b) CL images of YTT quartz crystals with zone of transect marked by red rectangle; scale bar represents 500 μm.

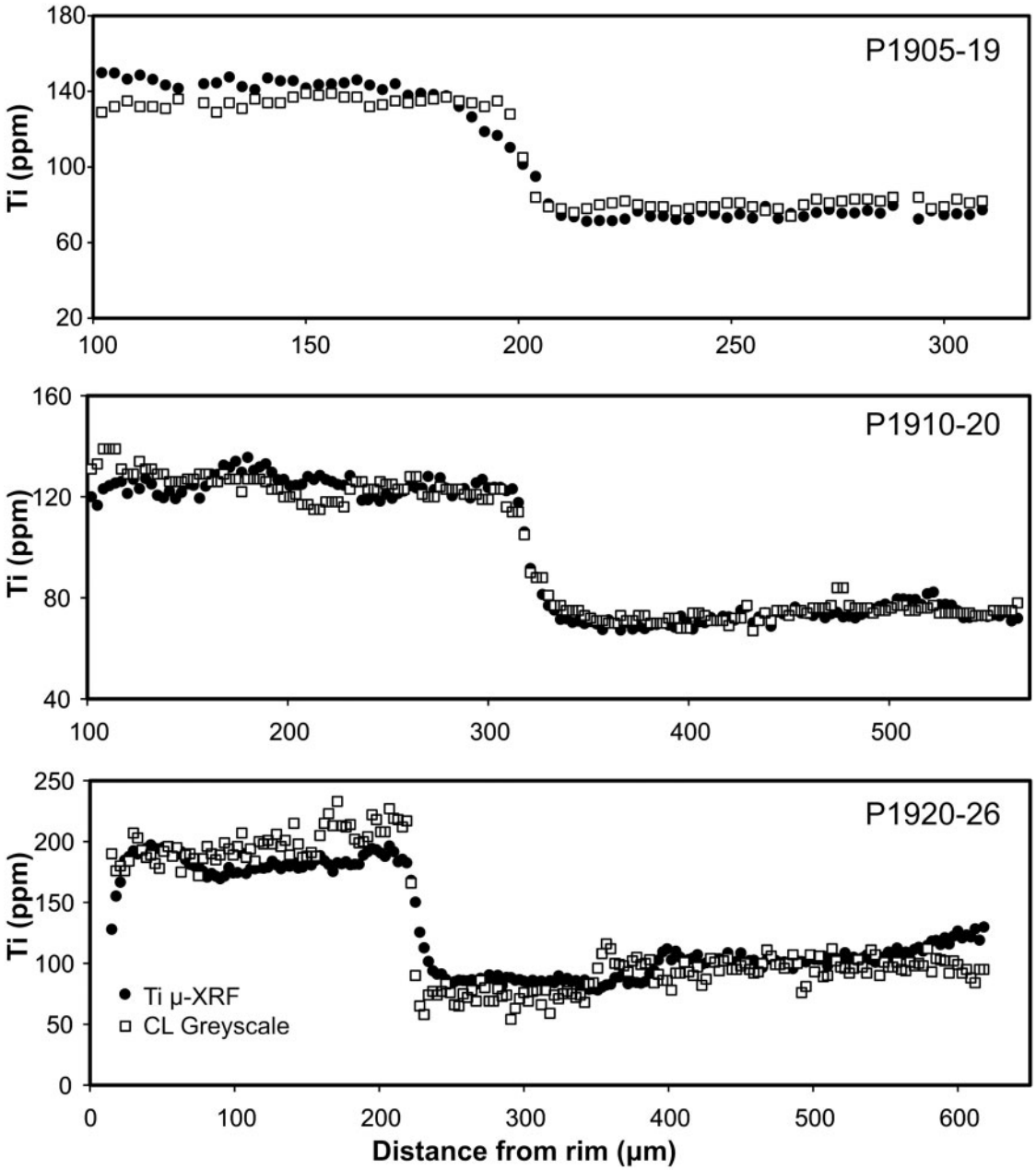

Fig. 9. Comparison of Ti μ-XRF data (black circles) and CL greyscale values (white squares) for three representative Whakamaru quartz crystals with distance from rim (same *y*-axis scales apply). These plots show the degree of agreement achievable between μ-XRF and CL techniques in describing the Ti concentration step. Two corrections were required to achieve this comparison: (1) for the offset evident in Figs 7 and 8 caused by the angle of μ-XRF beam penetration (by moving one of the profiles sideways); (2) for the depth-averaging nature of μ-XRF measurements by applying empirical scaling factors (one for each sample).

the 1D methods and 2D LB method and the angles used in the calculations. The advantages and disadvantages of each method are discussed in detail here.

1D analytical approach and 1D corrected method

Traditional 1D diffusion modeling across a crystal boundary assumes that diffusion occurs only along one direction (Morgan *et al.*, 2004; Smith *et al.*, 2010), which is clearly a simplification given the 3D structure of crystals. All timescale estimates represent maximum relaxation times owing to the assumption of an initial step function. The 1D modeling yields diffusion times for the core–rim boundary in quartz as follows: Whakamaru 20–300 years; YTT 100–450 years; EQF 10–1000 years (Table 3). Both

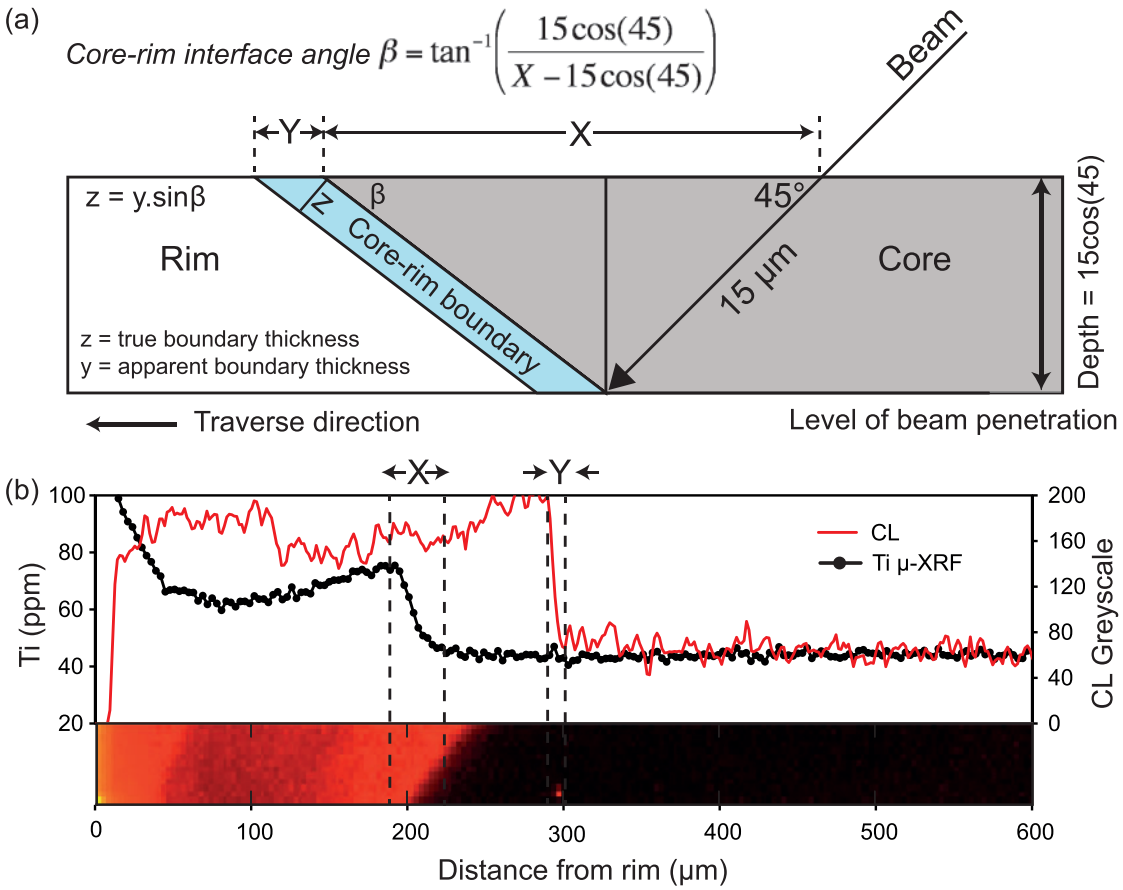

Fig. 10. Schematic cross-section through a quartz crystal in an epoxy mount, showing calculation of the angle (β) of the core–rim boundary with respect to the analysis surface. To account for the angle of the core–rim boundary with respect to the surface CL view of the diffusion boundary, we calculate the true distance across which the compositional step takes place (*z*) as indicated in (a) where the distance *Y* is determined as indicated by (b). [Note the 'averaging-effect' of the synchrotron beam as it penetrates 15 μm into the crystal (b), thus effectively depth-averaging Ti concentrations (black), and making the compositional step artificially shallower and less abrupt than shown by CL greyscale (red).]

1D methods allow calculation of time in a purely analytical fashion, with no numerical modeling involved.

Importantly, the 'corrected' analytical method used here accounts for the angle between the profile and the gradient [also accounted for by Costa & Morgan (2010)], and therefore provides a more accurate estimation of the range of possible diffusion times. On this basis, the core–rim boundary for Whakamaru quartz yields a time range of 20–245 years, with a median of ~80 years (Table 3). YTT rim boundaries provide a similar range of 40–300 years, with a median of 80 years; and EQF rim boundaries yield a range of 8–60 years, with a median of 30 years and one anomalous boundary of 1000 years (Table 3). This new 1D analytical approach provides a useful means of examining each point across the diffusion boundary with multiple times extracted, thus providing information on how good the fit is, the quality of the data, and the asymmetry of the profile around the midpoint. Anomalous points along the profile relate to structural defects or complexities in initial concentrations.

2D Lattice Boltzmann methodology

Results of 2D LB diffusion modeling (Table 3; accounting for the angle of core–rim boundary at depth, β), are illustrated with selected examples of Whakamaru quartz diffusion in Fig. 11, and EQF and YTT in Fig. 12. Two-dimensional LB diffusion calculations based on calibrated CL greyscale data generate a median diffusion time (to produce the significant core–rim elemental gradient) of 45 years for Whakamaru (average of 40 years, range of 10–60 years), 45 years for EQF (25–2450 years), and 70 years for YTT quartz (50–245 years; Table 3). A minor population of crystals yield longer diffusion times for the core–rim boundary as follows: YTT 245 years (Fig. 12e) and 200 years (Fig. 12f); EQF 2450 years (Fig. 12b; Table 3) and 140 years (Fig. 12c).

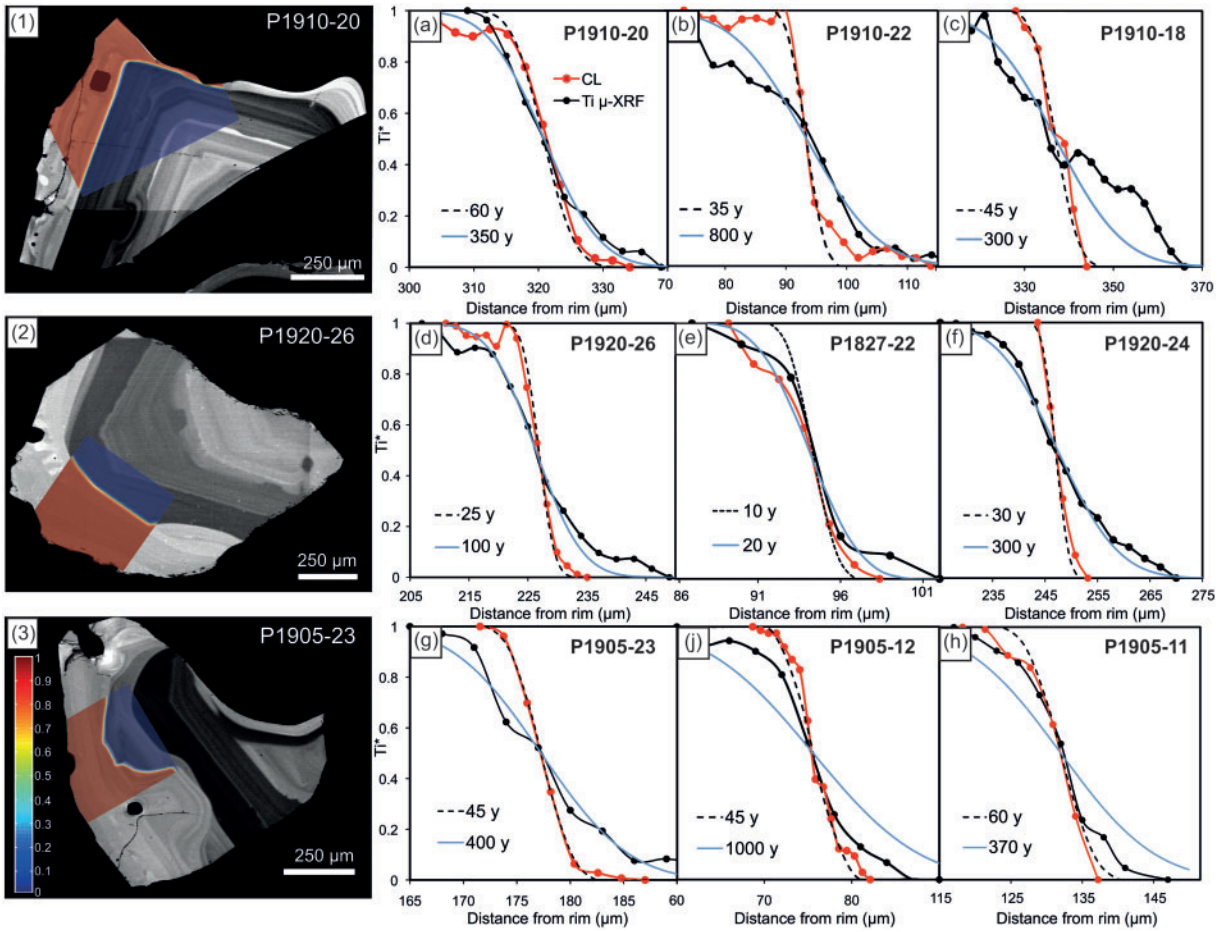

Fig. 11. Two-dimensional LB diffusion modeling for Whakamaru quartz; (1–3) CL images of quartz crystals showing area for 2D diffusion modeling, where dark-CL quartz cores (low-Ti) are coded blue, and bright-CL (high-Ti) rims are red. Colour scale (in image 3) shows normalized Ti where red (1) indicates maximum Ti concentrations (normalized concentration, $C^*=1$), and blue represents minimum Ti ($C^*=0$); (a–i) 2D LB diffusion profiles of Ti-in-quartz across the core–rim interface for selected quartz crystals. The black line shows Ti μ-XRF synchrotron data, red line indicates CL greyscale data and 2D LB model data are represented by dashed black lines (best fit) and blue lines. Results of 2D LB diffusion are corrected for angle (β) of the core–rim interface at depth (refer to Table 3). It should be noted that the μ-XRF data display a lack of smoothness owing to the depth-averaging effect.

The main advantage of this numerical method of diffusion modeling is that it accounts for the complex 2D crystal geometry and the angle between the profile and the modeled boundary (Fig. 13; see modeled areas of quartz crystals in Figs 11 and 12; with the addition of μ-XRF data we are also able to account for the 3D effect of the angle relative to the surface). Considering the complexities of the core–rim boundary observed for many quartz crystals, this 2D approach is likely to be more accurate than the 1D approach. For example, 2D modeling of diffusion across a corner transect (P1910-20; Figs 11a and 13) provides a significantly shorter timescale than the 1D methods (60 years by 2D vs 230 years by 1D; Table 3). This method also accounts for internal structure adjacent to the crystal boundary (e.g. P1905-23; Fig. 11g, P1905-12; Fig. 7), where structural complexities on the resorption surface result in a significant difference between 2D and 1D diffusion times. Although the 2D LB method is more robust, the results are essentially the same by all methods.

Synchrotron μ-XRF data for diffusion modeling

Although the high spatial resolution of Ti across the zone boundaries provided by μ-XRF is advantageous, diffusion modeling techniques applied to these data tend to result in longer diffusion times owing to the lower gradient of the compositional step (Figs 11 and 12). For example, the core–rim boundary of crystal P1910-18 (Fig. 11c) yields a diffusion time of 140 years from CL greyscale, whereas μ-XRF data indicate 540 years. The lower gradients reflect the angle of beam penetration and depth averaging of Ti during synchrotron analysis (Fig. 10). For this reason, greyscale calibrated CL values appear to more accurately

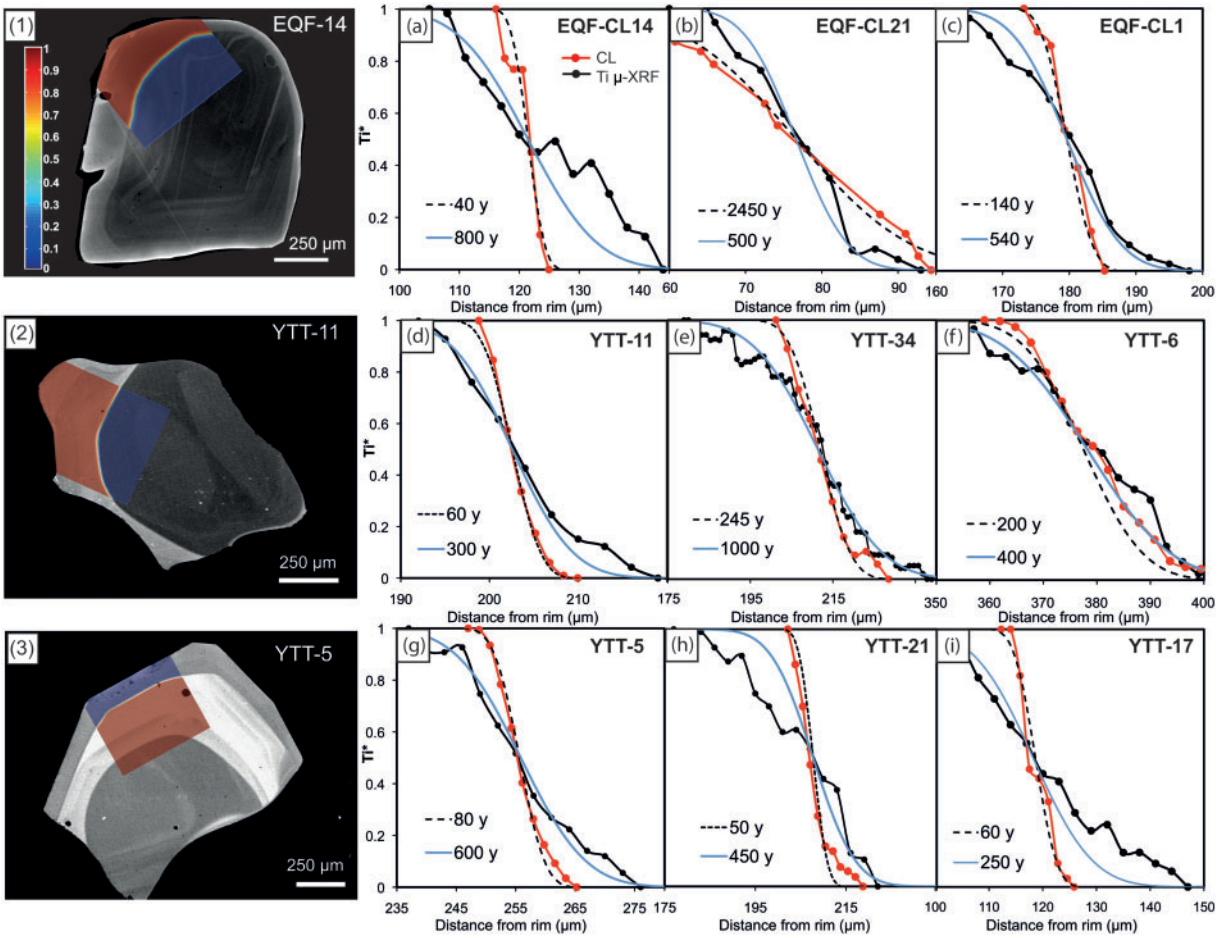

Fig. 12. (1–3) CL images of quartz crystals showing area for 2D diffusion modeling, where dark-CL quartz cores (low-Ti) are coded blue, and bright-CL (high-Ti) rims are red. Colour scale (in image 1) shows normalized Ti where red shows maximum Ti concentrations (normalized concentration, $C^* = 1$), and blue represents minimum Ti ($C^* = 0$); (a–i) 2D LB diffusion profiles of Ti-in-quartz across the core–rim interface for selected EQF and YTT quartz crystals. The black line shows Ti μ-XRF synchrotron data, red line indicates CL greyscale profile and 2D LB modeled lines are represented by dashed black lines (best fit) and blue lines. Results of 2D LB diffusion are corrected for angle (β) of the core–rim interface at depth (refer to Table 3). It should be noted that the μ-XRF data display a lack of smoothness owing to the depth-averaging effect.

indicate the compositional gradient and have been used here for the diffusion modeling. However, the spacing of the zones observed in the CL images is identical to that observed in the μ-XRF Ti data (Figs 7–9), confirming that Ti is the main CL activator in quartz. Furthermore, the μ-XRF data provide a useful means of calculating the angle of the core–rim interface, using the geometric constraints as outlined in Fig. 10. These angles are then incorporated into the diffusion modeling to constrain diffusion times (where the optimal diffusion transect is perpendicular to the core–rim boundary both at the surface and at depth).

Sources of error in diffusion time calculations

Possible sources of error in the diffusion calculations result from the assumptions outlined in the Methods section. The main source of uncertainty in the diffusion calculations is the choice of temperature, as small variations can result in very different timescales. The relationship between temperature and time is exponential (Fig. 14); for example, 1 year of diffusion at 800°C would take 25 years at 700°C, and 1100 years at 600°C [using equation (6)]. Costa *et al.* (2008) showed that the effect of changing temperature is less significant for activation energies of ~250 kJ mol^{-1}, however, and in particular if there are only temperature fluctuations around a mean rather than a prolonged heating or cooling trend. The temperature error is limited in this study owing to reliable constraints from Fe–Ti geothermometry, and the error arising from temperature estimations can be accounted for in the modeling (for example, refer to fig. 7 of Saunders *et al.*, 2010). The assumption that this temperature is fixed for diffusion

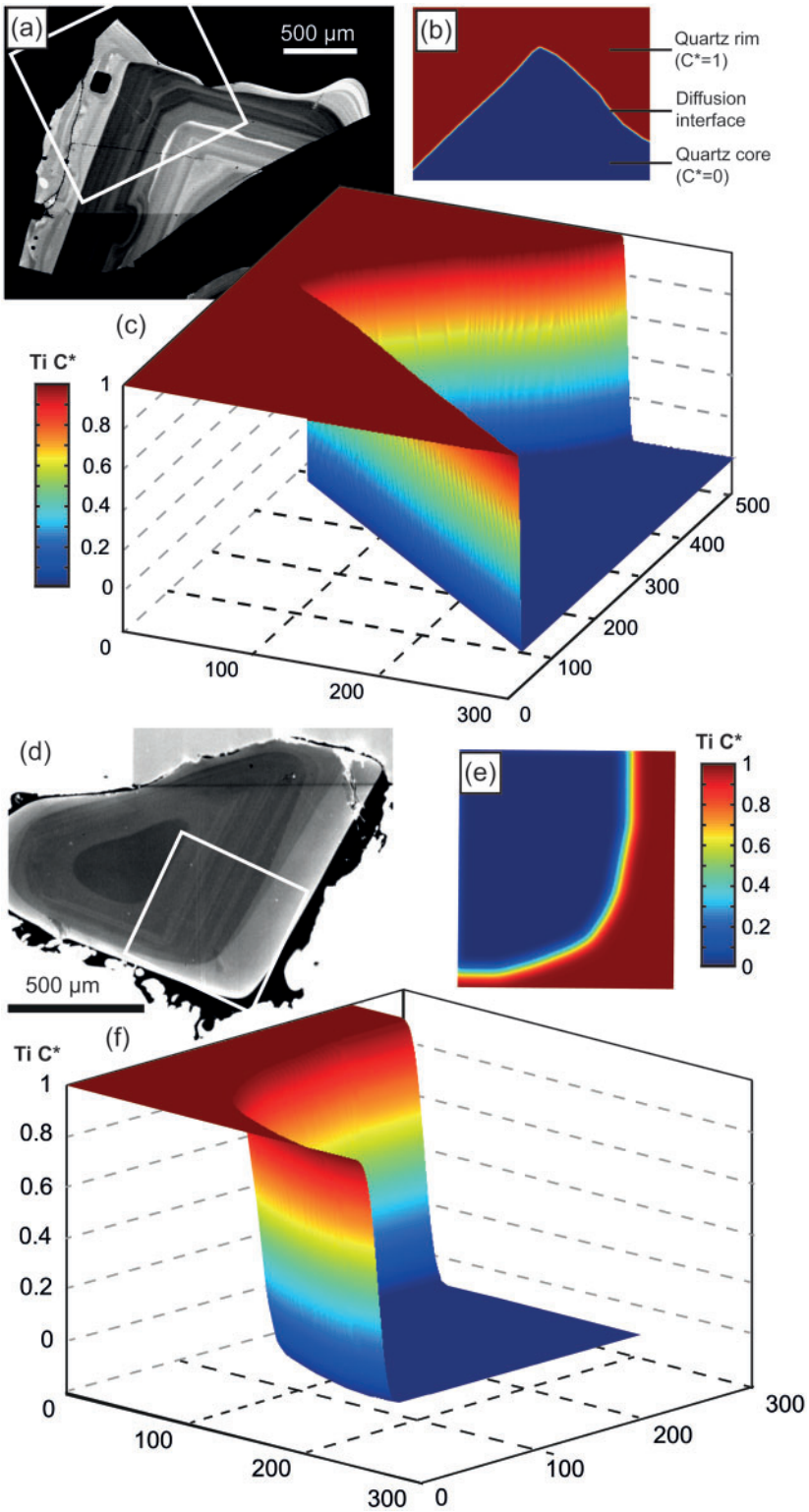

Fig. 13. Visualization of the 2D LB diffusion results. (a) CL image of quartz crystal P1910-20; white rectangle shows the area of the crystal that was modeled; (b) 2D LB output of crystal where blue represents quartz core (with normalized Ti concentrations, $C^* = 0$), and quartz rim coloured red ($C^* = 1$); (c) 3D visualization of the 2D LB output showing replication of complex 2D core–rim boundary morphology and the diffusion interface ($C^* = 0$–1); colour bar shows normalized Ti concentrations. The steep profile in (c) yields a diffusion time of 60 years; (d) CL image of quartz crystal EQF-2l; white rectangle shows the area of the crystal that was modeled; (e) 2D LB output of crystal; (f) 3D visualization of the 2D LB output showing replication of complex 2D core–rim boundary morphology and the diffusion interface. The profile yields a diffusion time of 2450 years.

is also an oversimplification, as diffusion would have continued during any thermal fluctuations prior to eruption (Shaw, 2004). As Fe–Ti oxide temperatures tend to be lower than TitaniQ rim temperatures for all three eruptions (Table 2), the timescales calculated using the eruption temperature are likely to be overestimated (although the direct comparability of Fe–Ti and TitaniQ temperatures is problematic, particularly given that TitaniQ requires assumptions of a_{TiO_2} and pressure, and the question of whether Fe–Ti oxides always record magmatic temperatures; Ghiorso & Evans, 2008). Overall uncertainty is attributed to two main factors here, curve fitting and temperature estimates (±10°C), and is shown in Table 3 as the quadratically combined total. There is also uncertainty on D_o (see Cherniak *et al.*, 2007), although this is less significant than the effect of temperature.

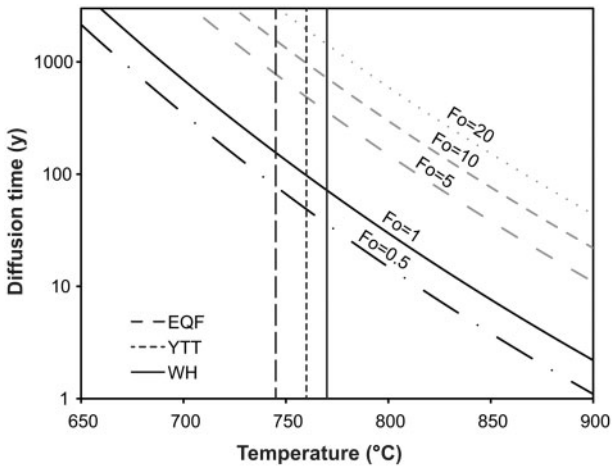

Fig. 14. Relationship between temperature and diffusion time for various Fo numbers (using the Arrhenius relationship for Ti diffusion in quartz from Cherniak *et al.*, 2007). Eruption temperatures for Whakamaru (WH), Earthquake Flat (EQF) and Younger Toba Tuff (YTT) are indicated by the black vertical lines. Most modeled quartz compositional steps give a Fo of 0·5–1 for Whakamaru (from CL greyscale as a proxy for Ti in quartz), corresponding to short diffusion times of ~10–60 years. For an eruption temperature of 770°C (relating to Whakamaru), diffusion times are as follows: Fo = 0·5, 35 years; Fo = 1, 70 years; Fo = 5, 360 years; Fo = 10, 720 years; Fo = 20, 1400 years. Modelled YTT and EQF profiles typically give a Fo of ~1, which corresponds to average diffusion times of 75–95 years and 120 years respectively (see Supplementary Material).

Furthermore, the primary assumption that the compositional step was initially vertical introduces an unquantifiable error into the diffusion calculations and means that the calculated diffusion times represent the maximum time since the rim grew and eruption. The timescales may also be an overestimation of the real times if part of the compositional profile is due to changing conditions during growth rather than diffusion alone (e.g. Costa & Morgan, 2010). The effect of the orientation of the crystal and zonation (owing to off-centre sectioning) with respect to the plane of analysis must also be considered (see Costa & Morgan, 2010). Compositional traverses were taken perpendicular to crystal margins where possible (see Costa *et al.*, 2008), and in one dimension we account for any angle between the zonation and the analysis transect (which would result in artificial lengthening of the profile). One-dimensional diffusion modeling cannot, however, account for the 2D structural complexities. Diffusion times calculated by the 2D LB method are shorter (Fig. 15)

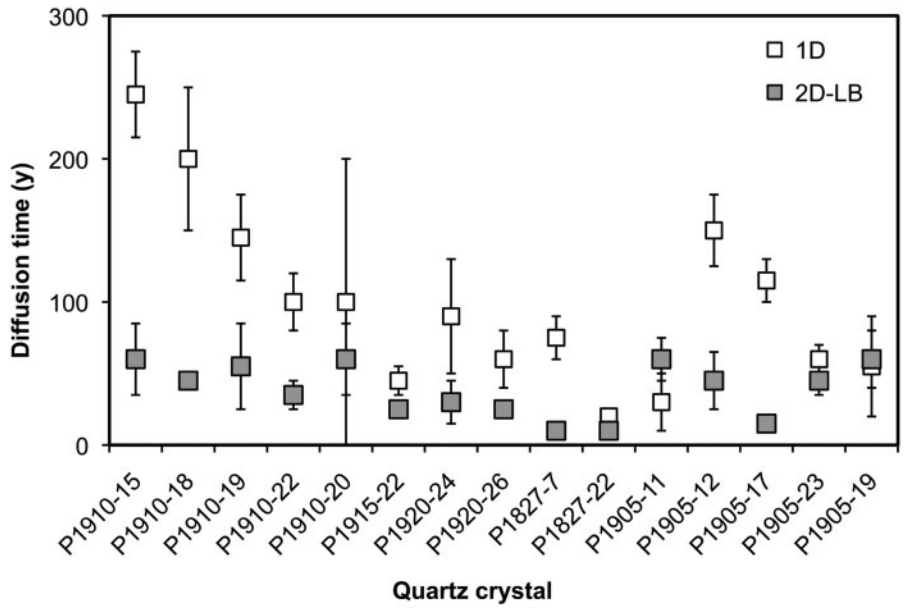

Fig. 15. Comparison of diffusion timescales for Whakamaru quartz derived by 1D method and 2D LB method (both angle-corrected). Uncertainties are from the modelling-fit procedure only (all are calculated at same temperature; see Table 3 for data).

because the method accounts for the flux coming from two directions and therefore equilibrium occurs faster [as outlined by Costa *et al.* (2003, 2008)]. Although 2D structural irregularities in the crystal boundary have been accounted for with the LB modeling, 3D effects are more difficult to assess and introduce an unquantifiable error (the overall effect is to make the estimates maximum estimates, similar to the 'lengthening' in one dimension). As outlined above, the synchrotron data can be used to calculate the angles of the core–rim boundary with respect to the surface, and this is built into the diffusion modeling, assuming that the core–rim interface is a planar feature at depth.

Stirring and reactivation timescales

The calculated stirring timescale [τ_m, see equation (15)] for the Whakamaru magma system is of the order of months to 1 year and refers to the time required to homogenize the entire magma chamber in response to the basaltic recharge event, once convection is fully developed (Huber *et al.*, 2009). The time required for reactivation of the Whakamaru crystal-rich magma reservoir is estimated as being of the order of 10^3–10^4 years (Huber *et al.*, 2012).

DISCUSSION

Modeling of quartz zonation patterns for three eruptions of varying magnitude provides information on the evolution of each magmatic system in terms of both physical and chemical changes.

Timescales of magma recharge

The variation in Ti concentration from synchrotron Ti maps and profiles (Figs 7–9) correlates with CL greyscale profiles as described above, confirming that CL intensity is directly proportional to Ti content (Götze *et al.*, 2001; Wark & Spear, 2005) and can be used as a proxy for Ti content. The relatively sharp compositional steps in these Ti maps and CL quartz profiles indicate that the Whakamaru, YTT and EQF magmas experienced a sudden physico-chemical change resulting in the resorption and subsequent overgrowth of high-Ti quartz rims. Timescales derived for these compositional changes are interpreted as the elapsed time between a significant magma recharge event (responsible for generating the thermal pulse indicated by the high-Ti quartz rims) and eruption, minus an unquantifiable period of time associated with rim resorption.

Two-dimensional LB diffusion modeling across this significant core–rim boundary yields a range of diffusion times, suggesting that some crystals record a unique history. The majority of Whakamaru quartz crystals modeled, however, indicate that the compositional step relates to a significant event that occurred 10–60 years prior to eruption (Table 3; Fig. 15). During this short time span, rapid rim growth must have occurred, followed by partial dissolution of the new quartz zone. This may have been coincident with volatile sparging from underlying mafic magma inputs, which possibly also destabilized the magma reservoir, ultimately leading to eruption. In comparison, 2D diffusion modeling of YTT quartz rims gave a diffusion timescale of 50–245 years, and 25–140 years for EQF quartz (Table 3), indicating that these major thermal–pressure–composition events can indeed occur rapidly in large-volume silicic systems. Given that the calculated timescales are all maximum estimates, however, the agreement may simply be related to the fact that results are close to the detection limit (decadal timescales) of the methods.

For the YTT and EQF eruptions some quartz core–rim boundaries yield longer times, which correspond to earlier events. An anomalous EQF crystal records an event 2450 years before eruption (EQF-CL21, Table 3 and Fig. 12b). Toba quartz crystals generally record a 60–80 year event (Table 3), with the exception of some crystals that record a 200–245 year event (YTT-34 and YTT-6; Table 3). The older timescales are thought to represent earlier magma recharge events that did not provide enough energy to fully prime the system for eruption, and indicate gradual magma accumulation. Whakamaru quartz records only short timescales of 10–60 years (2D LB data, Table 3) and therefore seems to record a more consistent history of compositional–thermal changes in the chamber. The short timescales yielded by Whakamaru quartz crystals suggest that the event that generated the significant core–rim compositional step most probably represents that which primed the magma for eruption.

Timescales of stirring and reactivation

Interpretations of magmatic timescales presented here are based on mafic magma recharging the silicic chamber, causing P–T changes (as recorded by compositional steps in quartz crystals), and initiating stirring and reactivation. Our thermodynamic calculations [equation (19)] suggest that the time required for reactivation (chamber-wide convection) of a voluminous crystal-rich magma reservoir, in response to mafic recharge, is of the order of 10^3–10^4 years, whereas stirring timescales [to completely homogenize the chamber; equations (15)–(18)] are <1 year. This implies that the magma chamber is much quicker to mix than it is to reactivate. As both processes are concurrent during most of the reactivation process (as soon as the reactivated part is able to convect), reactivated magmas tend to be homogeneous (see Huber *et al.*, 2012). These timescales thus provide a broader view of magma chamber development, which adds to the quartz-derived timescale. In contrast, studies of zircon crystallization histories for the Whakamaru magma system indicate magma generation and residence times over 250 ka (Brown &

Fletcher, 1999), highlighting the longevity of the system. The timescales of reheating and eruption-triggering events, as indicated by the quartz zoning, are very rapid in comparison (most probably <35 years for Whakamaru), and indicate that there must be a significant input of energy into the system to prime a large, crystal-rich silicic system for eruption.

Recharge episodicity: incremental magma accumulation

The diffusion timescales provide an insight into the episodicity of the recharge events responsible for significant P–T changes as reflected by quartz crystallization. The range of timescales is interpreted as providing a chronological record of magma intrusion during the later stages of magma chamber assembly. The final recharge event causes quartz rim resorption, and most probably represents the event that primed the system for eruption, although the timescale associated with this cannot be quantified by quartz diffusion modeling owing to rim resorption. Modeling results for Whakamaru quartz indicate significant recharge events during the period ~10–60 years prior to eruption (as recorded by all of the quartz crystals analysed; Table 3; assuming a constant temperature). The older timescales yielded by some YTT and EQF quartz crystals further highlight the role of incremental magma intrusions in the building up of large volumes of silicic magma.

Independent petrographic and geochemical data indicate that injections of mafic magma are the most likely explanation for the quartz resorption events and P–T change. Increasingly diffuse resorption horizons are preserved within quartz cores and some rims (e.g. 2450 years, EQF-CL21; Table 3), and these are best explained as being related to pockets of melt, partially isolated within the mushy system, which record subtly different crystallization histories. Furthermore, the quartz record indicates that most recharge events only temporarily perturb the system prior to further crystallization. Whether or not a recharge event results in an eruption is likely to depend on differences in melt composition, crystallinity, temperature, volatile content and the degree of interaction between the rhyolite and the intruding mafic magma. The presence of mafic-mingled pumices in all three eruptions indicates direct interaction between the two magmas, which may have primed the system for eruption. Similarly complex magmatic histories involving multiple recharge events and mafic–silicic interaction have been observed for magma systems of all sizes (e.g. El Chichón, Mexico: Davidson *et al.*, 2001; Andrews *et al.*, 2008; Nevado de Toluca, Mexico: Smith *et al.*, 2009; Tarawera, New Zealand: Shane *et al.*, 2007; Yellowstone caldera: Girard & Stix, 2009, 2010).

CONCLUSIONS

The new use of synchrotron techniques outlined in this study has shown that Ti transects correlate directly with CL profiles; this provides further evidence that Ti is the main activator of CL in quartz and adds robustness to the use of CL greyscale in Ti-in-quartz diffusion modeling. Chemical and textural zonation of quartz crystals from three major rhyolitic eruptions has indicated that a common feature of such systems is a sudden pre-eruption change in magmatic P–T conditions, resulting in high-Ti overgrowths on quartz crystals. Our calculations of timescales suggest that subsequent rejuvenation of the system occurred over a period of 10^3–10^4 years with stirring over <1 year required to completely homogenize the chamber.

The application of the new 2D diffusion modeling technique captures the geometry of the diffusion boundary more comprehensively than traditional 1D approaches. This approach takes into consideration the structural complexities of crystal boundaries and the angle of the diffusion profile to the boundary at depth, thus providing more reliable (and shorter) diffusion times. The calculated median timescales are 45 years for Whakamaru, 70 years for YTT and 45 years for EQF. These timescales reflect high-Ti crystallization, with the time between magma replenishment and eruption being longer as the P–T conditions had to change to bring quartz back into its stability field. These are maximum estimates, so the timescales of rim formation are potentially much shorter than the decadal to centennial timescales calculated. The range in diffusion timescales provides evidence for episodic magma recharge events and points to incremental growth of large-volume magma reservoirs.

Results of the 2D diffusion modeling applied to CL greyscale data show that the large-volume YTT and Whakamaru eruptions, and the small-volume EQF eruption, are characterized by remarkably similar diffusion times (all maximum estimates). This indicates that the time between the onset of crystallization after the reheating event and eruption is irrespective of magma volume, which has important implications for magma chamber dynamics and recharge mechanisms. The final recharge event recorded by quartz from all three magmatic systems is likely to have primed the magma for eruption, but the timescale calculations suggest that these events are unlikely to have been the eruption-triggering mechanism (although with maximum estimates, this cannot be discounted). We suggest that the spacing of magma recharge events, volatile transfer and rheology of the two magmas are likely to be crucial factors in determining whether a major recharge event will result in caldera-forming eruption rather than a temporary perturbation of the magmatic system. A comparison of the stirring–mixing and reactivation timescales indicates that the crystal-rich magma is expected to be homogeneous by the time it is

fully reactivated before the eruption. This study provides further evidence that silicic magma bodies are the result of extended periods of stirring, mixing and reactivation of crystal mush bodies, followed by significant thermal pulses attributed to magma recharge events that remobilize the magma and prime it for eruption.

ACKNOWLEDGEMENTS

We acknowledge the assistance of Diamond Beamline scientists and staff. In particular, Tina Geraki is thanked for her support and scientific input at Diamond Light Source on beamline I18. Kim Berlo is thanked for her help in collecting synchrotron Ti transects. We thank Stuart Kearns for his help with collecting CL imagery at the University of Bristol. Norman Charnley, University of Oxford, is thanked for his assistance with EMPA. Nick Pearce, Aberystwyth University, is thanked for providing the Toba sample and for help with LA-ICP-MS data acquisition. We thank Fidel Costa, Guilherme Gualda and Dan Morgan for their helpful reviews, which significantly improved this paper. Colin Wilson is acknowledged for helpful discussions and invaluable insight into TVZ volcanism.

FUNDING

This work was carried out with the support of the Diamond Light Source, Beamline I18 (experiment number 4842). N. Matthews was supported by a Woolf Fisher Trust Scholarship, New Zealand.

SUPPLEMENTARY DATA

Supplementary data for this paper are available at *Journal of Petrology* online.

REFERENCES

Andrews, B. J., Gardner, J. E. & Housh, T. B. (2008). Repeated recharge, assimilation, and hybridization in magmas erupted from El Chichón as recorded by plagioclase and amphibole phenocrysts. *Journal of Volcanology and Geothermal Research* **175**, 415–426.

Bachmann, O. & Bergantz, G. W. (2004). On the origin of crystal-poor rhyolites: extracted from batholithic crystal mushes. *Journal of Petrology* **45(8)**, 1565–1582.

Bachmann, O. & Bergantz, G. W. (2006). Gas percolation in upper-crustal silicic crystal mushes as a mechanism for upward heat advection and rejuvenation of near-solidus magma bodies. *Journal of Volcanology and Geothermal Research* **149**, 85–102.

Best, M. G. & Christiansen, E. H. (1997). Origin of broken phenocrysts in ash-flow tuffs. *Geological Society of America Bulletin* **109**, 63–73.

Bhatnagar, P., Gross, E. & Krook, A. (1954). A model for collisional processes in gases I: small amplitude processes in charged and neutral one component systems. *Physical Review* **94**, 511–525.

Bibby, H. M., Caldwell, T. G., Davey, F. J. & Webb, T. H. (1995). Geophysical evidence on the structure of the Taupo Volcanic Zone and its hydrothermal circulation. *Journal of Volcanology and Geothermal Research* **68**, 29–58.

Bindeman, I. (2005). Fragmentation phenomena in populations of magmatic crystals. *American Mineralogist* **90**, 1801–1815.

Blake, S. & Ivey, G. N. (1986). Magma-mixing and the dynamics of withdrawal from stratified reservoirs. *Journal of Volcanology and Geothermal Research* **27**, 153–178.

Blake, S., Wilson, C. J. N., Smith, I. E. M. & Walker, G. P. L. (1992). Petrology and dynamics of the Waimihia mixed magma eruption, Taupo Volcano, New Zealand. *Journal of the Geological Society, London* **149**, 193–207.

Briggs, N. D. (1976). Recognition and correlation of subdivisions within the Whakamaru Ignimbrite, central North Island, New Zealand. *New Zealand Journal of Geology and Geophysics* **19**, 463–501.

Brown, S. J. A. & Fletcher, I. R. (1999). SHRIMP U–Pb dating of the preeruption growth history of zircons from the 340 ka Whakamaru Ignimbrite, New Zealand: Evidence for >250 k.y. magma residence times. *Geology* **27**, 1035–1038.

Brown, S. J. A., Wilson, C. J. N., Cole, J. W. & Wooden, J. (1998). The Whakamaru group ignimbrites, Taupo Volcanic Zone, New Zealand: evidence for reverse tapping of a zoned silicic magmatic system. *Journal of Volcanology and Geothermal Research* **84**, 1–37.

Bryan, C. J., Sherburn, S., Bibby, H. M., Bannister, S. & Hurst, A. W. (1999). Shallow seismicity of the central Taupo Volcanic Zone, New Zealand: its distribution and nature. *New Zealand Journal of Geology and Geophysics* **42**, 533–542.

Charlier, B. L. A., Peate, D. W., Wilson, C. J. N., Lowenstern, J. B., Storey, M. & Brown, S. J. A. (2003). Crystallisation ages in coeval silicic magma bodies: ^{238}U–^{230}Th disequilibrium evidence from the Rotoiti and Earthquake Flat eruption deposits, Taupo Volcanic Zone, New Zealand. *Earth and Planetary Science Letters* **206**, 441–457.

Charlier, B. L. A., Wilson, C. J. N. & Davidson, J. P. (2008). Rapid open-system assembly of a large silicic magma body: time-resolved evidence from cored plagioclase crystals in the Oruanui eruption deposits, New Zealand. *Contributions to Mineralogy and Petrology* **156**, 799–813.

Charlier, B. L. A., Wilson, C. J. N. & Mortimer, N. (2010). Evidence from zircon U–Pb age spectra for crustal structure and felsic magma genesis at Taupo volcano, New Zealand. *Geology* **38**, 915–918.

Cherniak, D. J., Watson, E. B. & Wark, D. A. (2007). Ti diffusion in quartz. *Chemical Geology* **236**, 65–74.

Chesner, C. A. (1998). Petrogenesis of the Toba Tuffs, Sumatra, Indonesia. *Journal of Petrology* **39**, 397–438.

Chesner, C. A. & Luhr, J. F. (2010). A melt inclusion study of the Toba Tuffs, Sumatra, Indonesia. *Journal of Volcanology and Geothermal Research* **197(1–4)**, 259–278.

Chesner, C. A. & Rose, W. I. (1991). Stratigraphy of the Toba Tuffs and the evolution of the Toba Caldera Complex, Sumatra, Indonesia. *Bulletin of Volcanology* **53**, 343–356.

Chopard, B. & Droz, M. (1998). *Cellular Automata and Modeling of Physical Systems. Monographs and Texts in Statistical Physics*. Cambridge: Cambridge University Press.

Cole, J. W. (1990). Structural control and origin of volcanism in the Taupo Volcanic Zone, New Zealand. *Bulletin of Volcanology* **52**, 445–459.

Coltice, N. & Schmalzl, J. (2006). Mixing times in the mantle of the early Earth derived from 2-D and 3-D numerical simulations of convection. *Geophysical Research Letters* **33**, L23304, doi:10.1029/2006GL027707.

Coombs, M. L., Eichelberger, J. C. & Rutherford, M. J. (2000). Magma storage and mixing conditions for the 1953–1974 eruptions of Southwest Trident volcano, Katmai National Park, Alaska. *Contributions to Mineralogy and Petrology* **140**, 99–118.

Costa, F., Chakraborty, S. & Dohmen, R. (2003). Diffusion coupling between trace and major elements and a model for calculation of magma residence times using plagioclase. *Geochimica et Cosmochimica Acta* **67(12)**, 2189–2200.

Costa, F. & Chakraborty, S. (2004). Decadal time gaps between mafic intrusion and silicic eruption obtained from chemical zoning patterns in olivine. *Earth and Planetary Science Letters* **227**, 517–530, doi:10.1016/j.epsl.2004.08.011.

Costa, F. & Dungan, M. (2005). Short time scales of magmatic assimilation from diffusion modeling of multiple elements in olivine. *Geology* **33(1)**, 837–840.

Costa, F. & Morgan, D. (2010). Time constraints from chemical equilibration in magmatic crystals. In: Dosseto, A., Turner, S. P. & Van Orman, J. A. (eds) *Timescales of Magmatic Processes: from Core to Atmosphere*. Chichester: Wiley-Blackwell, pp. 125–159.

Costa, F., Dohmen, R. & Chakraborty, S. (2008). Time scales of magmatic processes from modeling the zoning patterns of crystals. In: Putirka, K. D. & Tepley, F. J., III (eds) *Minerals, Inclusions and Volcanic Processes. Mineralogical Society of America and Geochemical Society, Reviews in Mineralogy and Geochemistry* **69**, 545–594.

Costa, F., Coogan, L. A. & Chakraborty, S. (2010). The timescales of magma mixing and mingling involving primitive melts and melt–mush interaction at mid-ocean ridges. *Contributions to Mineralogy and Petrology* **159**, 371–387.

Cottrell, E., Gardner, J. E. & Rutherford, M. J. (1999). Petrologic and experimental evidence for the movement and heating of the pre-eruptive Minoan rhyodacite (Santorini, Greece). *Contributions to Mineralogy and Petrology* **135**, 315–331.

Davidson, J., Tepley, F., Palacz, Z. & Meffan-Main, S. (2001). Magma recharge, contamination and residence times revealed by *in situ* laser ablation isotopic analysis of feldspar in volcanic rocks. *Earth and Planetary Science Letters* **184**, 427–442.

Ewart, A. (1965). Mineralogy and petrogenesis of the Whakamaru Ignimbrite in the Maraetai area of the Taupo Volcanic Zone, New Zealand. *New Zealand Journal of Geology and Geophysics* **8**, 611–677.

Gaither, T., Reid, M. R. & Vazquez, J. A. (2009). Geochemistry and temperatures recorded by zircon during the final stages of the Youngest Toba Tuff magma chamber, Sumatra, Indonesia. *American Geophysical Union Fall Meeting 2009*, abstract V51E-1779.

Ghiorso, M. S. (1990). Thermodynamic properties of hematite–ilmenite–geikielite solid solutions. *Contributions to Mineralogy and Petrology* **104**, 645–667.

Ghiorso, M. S. & Evans, B. W. (2008). Thermodynamics of rhombohedral oxide solid solutions and a revision of the Fe–Ti two-oxide geothermometer and oxygen-barometer. *American Journal of Science* **308**, 957–1039.

Girard, G. & Stix, J. (2009). Magma recharge and crystal mush rejuvenation associated with early post-collapse Upper Basin Member rhyolites, Yellowstone Caldera, Wyoming. *Journal of Petrology* **50(11)**, 2095–2125.

Girard, G. & Stix, J. (2010). Rapid extraction of discrete magma batches from a large differentiating magma chamber: the Central Plateau Member rhyolites, Yellowstone Caldera, Wyoming. *Contributions to Mineralogy and Petrology* **160**, 441–465, doi:10.1007/s00410-009-0487-1.

Gottsmann, J., Lavallée, Y., Marti, J. & Aguirre-Diaz, G. (2009). Magma–tectonic interaction and the eruption of silicic batholiths. *Earth and Planetary Science Letters* **284**, 426–434.

Götze, J., Plötze, M. & Habermann, D. (2001). Origin, spectral characteristics and practical applications of the cathodoluminescence (CL) of quartz—a review. *Mineralogy and Petrology* **71**, 225–250.

Götze, J., Plötze, M., Graupner, T., Hallbauer, D. K. & Bray, C. J. (2004). Trace element incorporation into quartz: A combined study by ICP-MS, electron spin resonance, cathodoluminescence, capillary ion analysis, and gas chromatography. *Geochimica et Cosmochimica Acta* **68**, 3741–3759.

Graham, I. J., Cole, J. W., Briggs, R. M., Gamble, J. A. & Smith, I. E. M. (1995). Petrology and petrogenesis of volcanic rocks from the Taupo Volcanic Zone: a review. *Journal of Volcanology and Geothermal Research* **68**, 59–87.

Gualda, G. A. R., Cook, D. L., Chopra, R., Qin, L., Anderson, A. T. & Rivers, M. (2004). Fragmentation, nucleation and migration of crystals and bubbles in the Bishop Tuff rhyolitic magma. *Transactions of the Royal Society of Edinburgh, Earth Sciences* **95**, 375–390.

Harrison, A. J. & White, R. S. (2004). Crustal structure of the Taupo Volcanic Zone, New Zealand: stretching and igneous intrusion. *Geophysical Research Letters* **31**, L13615, doi:10.1029/2004GL019885.

Hildreth, W. (1981). Gradients in silicic magma chambers: implications for lithospheric magmatism. *Journal of Geophysical Research* **86**, 10153–10192.

Hildreth, W. (2004). Volcanological perspectives on Long Valley, Mammoth Mountain, and Mono Craters: several contiguous but discrete systems. *Journal of Volcanology and Geothermal Research* **136**, 169–198.

Hochstein, M. P. (1995). Crustal heat transfer in the Taupo Volcanic Zone (New Zealand): comparison with other volcanic arcs and explanatory heat source models. *Journal of Volcanology and Geothermal Research* **68**, 117–151.

Holland, T. J. B. & Powell, R. (1998). An internally consistent thermodynamic data set for phases of petrological interest. *Journal of Metamorphic Geology* **16**, 309–343.

Huber, C., Parmigiani, A., Chopard, B., Manga, M. & Bachmann, O. (2008). Lattice Boltzmann model for melting with natural convection. *International Journal of Heat and Fluid Flow* **29**, 1469–1480.

Huber, C., Bachmann, O. & Manga, M. (2009). Homogenization processes in silicic magma chambers by stirring and mushification (latent heat buffering). *Earth and Planetary Science Letters* **283**, 38–47.

Huber, C., Chopard, B. & Manga, M. (2010*a*). A lattice Boltzmann model for coupled diffusion. *Journal of Computational Physics* **229**, 7956–7976.

Huber, C., Bachmann, O. & Dufek, J. (2010*b*). The limitations of melting on the reactivation of silicic mushes. *Journal of Volcanology and Geothermal Research* **195(2–4)**, 97–105.

Huber, C., Bachmann, O. & Manga, M. (2010*c*). Two competing effects of volatiles on heat transfer in crystal-rich magmas: thermal insulation vs defrosting. *Journal of Petrology* **51(4)**, 847–867.

Huber, C., Cassata, W. S. & Renne, P. R. (2011). A lattice-Boltzman model for noble gas diffusion in solids: The importance of domain shape and diffusive anisotropy and implications for thermochronometry. *Geochimica et Cosmochimica Acta* **75(8)**, 2170–2186.

Huber, C., Bachmann, O. & Dufek, J. (2012). Crystal-poor versus crystal-rich ignimbrites: a competition between stirring and reactivation. *Geology* **40**, 115–118.

Klügel, A. (2001). Prolonged reactions between harzburgite xenoliths and silica-undersaturated melt: Implications for dissolution and Fe–Mg interdiffusion rates of orthopyroxene. *Contributions to Mineralogy and Petrology* **141**, 1–14.

Leonard, G. S., Cole, J. W., Nairn, I. A. & Self, S. (2002). Basalt triggering of the *c.* AD 1305 Kaharoa rhyolite eruption, Tarawera Volcanic Complex, New Zealand. *Journal of Volcanology and Geothermal Research* **115**, 461–486.

Liu, Y., Anderson, A. T., Wilson, C. J. N., Davis, A. M. & Steele, I. M. (2006*a*). Mixing and differentiation in the Oruanui rhyolitic magma, Taupo, New Zealand: evidence from volatiles and trace

elements in melt inclusions. *Contributions to Mineralogy and Petrology* **151**, 71–87.

Liu, Z., Colin, C. & Trentesaux, A. (2006*b*). Major element geochemistry of glass shards and minerals in the Youngest Toba Tephra in the southwestern China Sea. *Journal of Asian Earth Sciences* **27**, 99–107.

Martin, R. C. (1965). Lithology and eruptive history of the Whakamaru Ignimbrites in the Maraetai area of the Taupo Volcanic Zone, New Zealand. *New Zealand Journal of Geology and Geophysics* **8**, 680–701.

Mason, B. G., Pyle, D. M. & Oppenheimer, C. (2004). The size and frequency of the largest explosive eruptions on Earth. *Bulletin of Volcanology* **66**, 735–748.

Matthews, N. E., Pyle, D. M., Smith, V. C., Wilson, C. J. N., Huber, C. & van Hinsberg, V. (2012). Quartz zoning and the pre-eruptive evolution of the ~340 ka Whakamaru magma systems, New Zealand. *Contributions to Mineralogy and Petrology* **163(1)**, 87–107, doi:10.1007/s00410-001-0660-1.

McCulloch, M. T., Kyser, T. K., Woodhead, J. D. & Kinsey, L. (1994). Pb–Sr–Nd–O isotopic constraints on the origin of rhyolites from the Taupo Volcanic Zone of New Zealand: evidence for assimilation followed by fractionation from basalt. *Contributions to Mineralogy and Petrology* **115**, 303–312.

Molloy, C., Shane, P. & Nairn, I. (2008). *Pre-eruption thermal rejuvenation and stirring of a partly crystalline pluton revealed by the Earthquake Flat Pyroclastics deposits, New Zealand*, London: Journal of the Geological Society **165**, 435–447.

Morgan, D. J. & Blake, S. (2006). Magmatic residence times of zoned phenocrysts: introduction and application of the binary element diffusion modeling (BEDM) technique. *Contributions to Mineralogy and Petrology* **151**, 58–70.

Morgan, D. J., Blake, S., Rogers, N. W. B., DeVivo, B., Rolandi, G., Macdonald, R. & Hawkesworth, C. J. (2004). Time scales of crystal residence and magma chamber volume from modelling of diffusion profiles in phenocrysts: Vesuvius 1944. *Earth and Planetary Science Letters* **222**, 933–946.

Mosselmans, J. F. W., Quinn, P. D., Roque-Rosell, J., Atkinson, K. D., Dent, A. J., Cavill, S. I., Hodson, M. E., Kirk, C. A. & Schofield, P. F. (2008). The first environmental science experiments on the new microfocus spectroscopy beamline at diamond. *Mineralogical Magazine* **72**, 197–200.

Mosselmans, J. F. W., Quinn, P. D., Dent, A. J., Cavill, S. A., Diaz Moreno, S., Peach, A., Leicester, P. J., Keylock, S. J., Gregory, S. R., Atkinson, K. D. & Roque Rosell, J. (2009). I18—the microfocus spectroscopy beamline at the Diamond light source. *Journal of Synchrotron Radiation* **16**, 818–824.

Nakamura, M. (1995). Continuous mixing of crystal mush and replenished magma in the ongoing Unzen eruption. *Geology* **23**, 807–810, doi:10.1130/0091-7613(1995)023<0807:CMOCMA>2.3.CO;2.

Pearce, N. J. G., Westgate, J. A. & Perkins, W. T. (1996). Developments in the analysis of volcanic glass shards by laser ablation ICP-MS: quantitative and single internal standard-multi-element methods. *Quaternary International* **34–36**, 213–227.

Pearce, N. J. G., Perkins, W. T., Westgate, J. A., Gorton, M. P., Jackson, S. E., Neal, C. R. & Chenery, S. P. (1997). A compilation of new and published major and trace element data for NIST SRM 610 and NIST SRM 612 glass reference materials. *Geostandards Newsletter* **21**, 115–144.

Pearce, N. J. G., Westgate, J. A., Perkins, W. T., Eastwood, W. J. & Shane, P. A. R. (1999). The application of laser ablation ICP-MS to the analysis of volcanic glass shards from tephra deposits: bulk glass and single shard analysis. *Global and Planetary Change* **21**, 151–171.

Pearce, N. J. G., Eastwood, W. J., Westgate, J. A. & Perkins, W. T. (2002). The composition of juvenile volcanic glass from the *c.* 3600 B.P. Minoan eruption of Santorini (Thera). *Journal of the Geological Society, London* **159**, 545–556.

Pearce, N. J. G., Westgate, J. A., Perkins, W. T. & Preece, S. J. (2004). The application of ICP-MS methods to tephrochronological problems. *Applied Geochemistry* **19**, 289–322.

Pearce, N. J. G., Perkins, W. T., Westgate, J. A. & Wade, S. C. (2011). Trace-element microanalysis by LA-ICP-MS: The quest for comprehensive chemical characterization of single, sub-10 μm volcanic glass shards. *Quaternary International* **246**, 57–81.

Peppard, B. T., Steele, I. M., Davis, A. M., Wallace, P. J. & Anderson, A. T. (2001). Zoned quartz phenocrysts from the rhyolitic Bishop Tuff. *American Mineralogist* **86**, 1034–1052.

Perkins, W. T. & Pearce, N. J. G. (1995). Mineral microanalysis by laserprobe inductively coupled plasma mass spectrometry. In: Potts, P. J., Bowles, J. F. W., Reed, S. J. B. & Cave, M. R. (eds) *Microprobe Techniques in the Earth Sciences*. London: Mineralogical Society, pp. 291–325.

Perkins, W. T., Pearce, N. J. G. & Westgate, J. A. (1997). The development of laser ablation ICP-MS and calibration strategies: examples from the analysis of trace elements in volcanic glass shards and sulphide minerals. *Geostandards Newsletter* **21**, 175–190.

Petrinovic, I. A., Marti, J., Aguirre-Diaz, G. J., Guzman, S., Geyer, A. & Salado Paz, N. (2010). The Cerro Aguas Calientes caldera, NW Argentina: An example of a tectonically controlled, polygenetic collapse caldera, and its regional significance. *Journal of Volcanology and Geothermal Research* **194**, 15–26.

Ravel, B. & Newville, M. (2005). ATHENA, ARTEMIS, HEPHAESTUS: data analysis for X-ray absorption spectroscopy using IFEFFIT. *Journal of Synchrotron Radiation* **12**, 537–541.

Reid, M. R., Vazquez, J. A. & Schmitt, A. K. (2010). Zircon-scale insights into the history of a supervolcano, Bishop Tuff, Long Valley, California, with implications for the Ti-in-zircon geothermometer. *Contributions to Mineralogy and Petrology* **161(2)**, 293–311, doi:10.1007/s00410-010-0532-0.

Ridolfi, F., Renzulli, A. & Puerini, M. (2010). Stability and chemical equilibrium of amphibole in calc-alkaline magmas: an overview, new thermobarometric formulations and application to subduction-related volcanoes. *Contributions to Mineralogy and Petrology* **160**, 45–66.

Rose, W. I. & Chesner, C. A. (1990). Worldwide dispersal of ash and gases from the Earth's largest known eruption: Toba, Sumatra, 75 ka. *Palaeogeography, Palaeoclimatology, Palaeoecology* **89**, 269–275.

Rusk, B. G., Lowers, H. A. & Reed, M. H. (2008). Trace elements in hydrothermal quartz: relationships to cathodoluminescent textures and insights into vein formation. *Geology* **36**, 547–550.

Saunders, K. E., Morgan, D. J., Baker, J. A. & Wysoczanski, R. J. (2010). The magmatic evolution of the Whakamaru superuption, New Zealand, constrained by a microanalytical study of plagioclase and quartz. *Journal of Petrology* **51(12)**, 2465–2488.

Scaillet, B., Holtz, F. & Pichavant, M. (1998). Phase equilibrium constraints on the viscosity of silicic magmas 1. Volcanic–plutonic comparison. *Journal of Geophysical Research* **103**, 257–266.

Schmitz, M. D. & Smith, I. E. M. (2004). The petrology of the Rotoiti eruption sequence, Taupo Volcanic Zone: an example of fractionation of a rhyolitic system. *Journal of Petrology* **45(10)**, 2045–2066.

Shane, P., Westgate, J., Williams, M. & Korisetar, R. (1995). New geochemical evidence for the Youngest Toba Tuff in India. *Quaternary Research* **44**, 200–204.

Shane, P., Martin, S. B., Smith, V. C., Beggs, K. F., Darragh, M. B., Cole, J. W. & Nairn, I. A. (2007). Multiple rhyolite magmas and

basalt injection in the 17·7 ka Rerewhakaaitu eruption episode from Tarawera volcanic complex, New Zealand. *Journal of Volcanology and Geothermal Research* **164**, 1–26.

Shane, P., Smith, V. C. & Nairn, I. A. (2008*a*). Millennial timescale resolution of rhyolite magma recharge at Tarawera volcano: insights from quartz chemistry and melt inclusions. *Contributions to Mineralogy and Petrology* **155**, 397–411.

Shane, P., Nairn, I. A., Smith, V. C., Darragh, M., Beggs, K. F. & Cole, J. W. (2008*b*). Silicic recharge of multiple rhyolite magmas by basaltic intrusion during the 22·6 ka Okaraka eruption episode, New Zealand. *Lithos* **103**, 527–549.

Shaw, C. (2004). The temporal evolution of three magmatic systems in the West Eifel volcanic field, Germany. *Journal of Volcanology and Geothermal Research* **131**, 213–240, doi:10.1016/S0377-0273(03)¥00363-9.

Smith, V. C., Shane, P. & Nairn, I. A. (2005). Trends in rhyolite geochemistry, mineralogy, and magma storage during the last 50 kyr at Okataina and Taupo volcanic centres, Taupo Volcanic Zone, New Zealand. *Journal of Volcanology and Geothermal Research* **148**, 372–406.

Smith, V. C., Blundy, J. D. & Arce, J. L. (2009). A temporal record of magma accumulation and evolution beneath Nevado de Toluca, Mexico, preserved in plagioclase phenocrysts. *Journal of Petrology* **50(3)**, 405–426, doi:10.1093/petrology/egp005.

Smith, V., Shane, P. & Nairn, I. (2010). Insights into silicic melt generation using plagioclase, quartz and melt inclusions from the caldera-forming Rotoiti eruption, Taupo Volcanic Zone, New Zealand. *Contributions to Mineralogy and Petrology* **160(6)**, 951–971, doi:10.1007/s00410-010-0516-0.

Smith, V. C., Pearce, N. J. G., Matthews, N. E., Westgate, J. A., Petraglia, M. D., Haslam, M., Lane, C. S., Korisettar, R. & Pal, J. N. (2011). Geochemical fingerprinting the widespread Toba tephra using biotite compositions. *Quaternary International* **246**, 97–104, doi:10.1016/j.quaint.2011.05.012.

Solé, V. A., Papillon, E., Cotte, M., Walter, P. & Susini, J. (2007). A multiplatform code for the analysis of energy-dispersive X-ray fluorescence spectra. *Spectrochimica Acta, Part B* **62**, 63–68.

Stern, T. A., Stratford, W. R. & Salmon, M. L. (2006). Subduction evolution and mantle dynamics at a continental margin: central North Island, New Zealand. *Reviews of Geophysics* **44**, RG4002, Paper 2005RG000171.

Stevens-Kalceff, M. A. (2009). Cathodoluminescence microcharacterization of point defects in α-quartz. *Mineralogical Magazine* **73(4)**, 585–605.

Stratford, W. R. & Stern, T. A. (2004). Strong seismic reflections and melts in the mantle of a continental back-arc basin. *Geophysical Research Letters* **31**, L06622, doi:10.1029/2003GL019232.

Tait, S. (1992). Selective preservation of melt inclusions in igneous phenocrysts. *American Mineralogist* **77**, 146–155.

Tait, S. R., Worner, G., van den Bogaard, P. & Schmincke, H. (1989). Cumulate nodules as evidence for convective fractionation in a phonolite magma chamber. *Journal of Volcanology and Geothermal Research* **37**, 21–37.

Thomas, J. B., Watson, E. B., Spear, F. S., Shemella, P. T., Nayak, S. K. & Lanzirotti, A. (2010). TitaniQ under pressure: the effect of pressure and temperature on the solubility of Ti in quartz. *Contributions to Mineralogy and Petrology* **160(5)**, 743–759, doi:10.1007/s00410-010-0505-3.

Turcotte, D. L. & Schubert, G. (2002). *Geodynamics*, 2nd edn. Cambridge: Cambridge University Press.

Vazquez, J. A. & Reid, M. R. (2004). Probing the accumulation history of the voluminous Toba magma. *Science* **305**, 991–994.

Wark, D. A. & Spear, F. S. (2005). Titanium in quartz: cathodoluminescence and thermometry. *Geochimica et Cosmochimica Acta, Supplement* **69**, A592.

Wark, D. A. & Watson, E. B. (2006). TitaniQ: a titanium-in-quartz geothermometer. *Contributions to Mineralogy and Petrology* **152**, 743–754.

Wark, D. A., Hildreth, W., Spear, F. S., Cherniak, D. J. & Watson, E. B. (2007). Pre-eruption recharge of the Bishop magma system. *Geology* **35**, 235–238.

Watt, G. R., Wright, P., Galloway, S. & McLean, C. (1997). Cathodoluminescence and trace element zoning in quartz phenocrysts and xenocrysts. *Geochimica et Cosmochimica Acta* **61**, 4337–4348.

Waychunas, G. A. (1987). Synchrotron radiation XANES spectroscopy of Ti in minerals: effects of Ti bonding distances, Ti valence and site geometry on absorption edge structure. *American Mineralogist* **72**, 89–101.

White, R. W., Powell, R. & Clarke, G. L. (2002). The interpretation of reaction textures in Fe-rich metapelitic granulites of the Musgrave Block, central Australia: constraints from mineral equilibria calculations in the system K_2O–FeO–MgO–Al_2O_3–SiO_2–H_2O–TiO_2–Fe_2O_3. *Journal of Metamorphic Geology* **20**, 41–55.

Wiebe, R. A., Wark, D. A. & Hawkins, D. P. (2007). Insights from quartz cathodoluminescence zoning into crystallization. *Contributions to Mineralogy and Petrology* **154**, 439–453.

Wilson, C. J. N., Houghton, B. F. & Lloyd, E. F. (1986). Volcanic history and evolution of the Maroa–Taupo area, central North Island. *Royal Society of New Zealand Bulletin* **23**, 194–223.

Wilson, C. J. N., Houghton, B. F., McWilliams, M. O., Lanphere, M. A., Weaver, S. D. & Briggs, R. M. (1995). Volcanic and structural evolution of Taupo Volcanic Zone, New Zealand: a review. *Journal of Volcanology and Geothermal Research* **68**, 1–28.

Wilson, C. J. N., Blake, S., Charlier, B. L. A. & Sutton, A. N. (2006). The 26·5 ka Oruanui eruption, Taupo volcano, New Zealand: development, characteristics and evacuation of a large rhyolitic magma body. *Journal of Petrology* **47**, 35–69.

Wilson, C. J. N., Gravley, D. M., Leonard, G. S. & Rowland, J. V. (2009). Volcanism in the central Taupo Volcanic Zone, New Zealand: tempo, styles and controls. In: Thordarson, T., Larsen, G., Self, S., Rowland, S. & Hoskuldsson, A. (eds) *Studies in Volcanology: The Legacy of George Walker.* Special Publications of IAVCEI 2. London: Geological Society, pp. 225–247.

Wilson, C. J. N., Seward, T. M., Allan, A. S. R., Charlier, B. L. A., Bellow, L. & Hildreth, W. (2012). TitaniQ under pressure: the effect of pressure and temperature on the solubility of Ti in quartz. In: J. B. Thomas, E. B. Watson, F. S. Spear, P. T. Shemella, S. K. Nayak, & A. Lanzirotti (eds) *Contributions to Mineralogy and Petrology* (in preparation).

Wolf-Gladrow, D. A. (2000). *Lattice-Gas Cellular Automata and lattice Boltzmann models: An Introduction.* Berlin: Springer, 308 p.

Zellmer, G. F., Blake, S., Vance, D., Hawkesworth, C. & Turner, S. (1999). Plagioclase residence times at two island arc volcanoes (Kameni Islands, Santorini and Soufrière, St. Vincent) determined by Sr diffusion systematics. *Contributions to Mineralogy and Petrology* **136**, 345–357.

APPENDIX A

The derivation for the 1D analytical method is described in Fig. A1. This method allows us to account for the angle between the diffusion transect and perpendicular to the core–rim boundary.

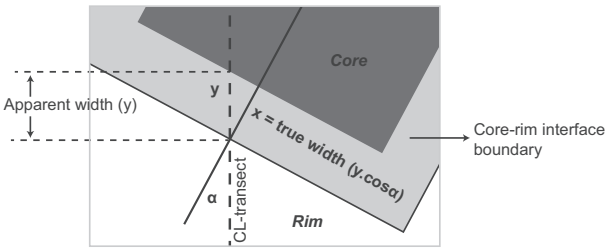

Fig. A1. Detail of the core–rim interface (plan view), where the dashed black line indicates the calibrated CL transect, and the black continuous line represents the ideal diffusion modeling profile, oriented perpendicular to the core–rim interface. To correct for this angle to the diffusion boundary we consider the 'true' and 'apparent' widths of the transition zone, where the ratio of true to apparent widths is given by $x/y = y\cos\alpha/y = \cos\alpha$ (where α is the angle to perpendicular from the core–rim boundary). Modified from Matthews *et al.*, 2012.

APPENDIX B: CALCULATION OF μ-XRF SYNCHROTRON BEAM PENETRATION

Calculation of the depth of beam penetration into the crystal specimen is based on the equation

$$I = I_o \exp(-\mu x) \quad \text{(A1)}$$

which describes the attenuation of X-rays by a material, where I_o is the original intensity of the signal, I is the resulting intensity after going through the material of thickness x, and μ is the mass attenuation coefficient of the absorber material. This depends on the atomic numbers of the main constituents, the average density and the energy of the X-rays. This is typically expressed as the maximum depth from which the signal is derived (x) as $I/I_o = 1/e$ (which equates to the depth for 65% of the signal).

Using quartz (SiO_2) as the main matrix, with a density of 2·6 g cm^{-3}, energy of the Ti signal of 4·5 keV, and the 45° beam angle, we calculate a penetration depth of ~15 μm.